

## Quarterly Technical Report

## Solid State Research

2000:3

---

**Lincoln Laboratory**  
MASSACHUSETTS INSTITUTE OF TECHNOLOGY  
*LEXINGTON, MASSACHUSETTS*

---



Prepared for the Department of the Air Force under Contract F19628-00-C-0002.

Approved for public release; distribution is unlimited.

20010326 018

This report is based on studies performed at Lincoln Laboratory, a center for research operated by Massachusetts Institute of Technology. The work was sponsored by the Department of the Air Force under Contract F19628-00-C-0002.

This report may be reproduced to satisfy needs of U.S. Government agencies.

The ESC Public Affairs Office has reviewed this report, and it is releasable to the National Technical Information Service, where it will be available to the general public, including foreign nationals.

This technical report has been reviewed and is approved for publication.

FOR THE COMMANDER



Gary Tutungian  
Administrative Contracting Officer  
Plans and Programs Directorate  
Contracted Support Management

Non-Lincoln Recipients

PLEASE DO NOT RETURN

Permission is given to destroy this document  
when it is no longer needed.

Massachusetts Institute of Technology  
Lincoln Laboratory

**Solid State Research**

**Quarterly Technical Report**

1 May—31 July 2000

Issued 16 February 2001

Approved for public release; distribution is unlimited.

Lexington

Massachusetts

## **ABSTRACT**

This report covers in detail the research work of the Solid State Division at Lincoln Laboratory for the period 1 May through 31 July 2000. The topics covered are Quantum Electronics, Electro-optical Materials and Devices, Submicrometer Technology, Biosensor and Molecular Technologies, Advanced Imaging Technology, Analog Device Technology, and Advanced Silicon Technology. Funding is provided by several DoD organizations—including the Air Force, Army, BMDO, DARPA, Navy, NSA, and OSD—and also by the DOE, NASA, and NIST.

## TABLE OF CONTENTS

Abstract	iii
List of Illustrations	vii
List of Tables	x
Introduction	xi
Reports on Solid State Research	xiii
Organization	xxv
 1. QUANTUM ELECTRONICS	 1
1.1 Miniature Eye-Safe Gain-Switched Laser for Ranging Applications	1
 2. ELECTRO-OPTICAL MATERIALS AND DEVICES	 7
2.1 Measurement of Nanometer Air Gaps in Semiconductor Wafer Bonding	7
 3. SUBMICROMETER TECHNOLOGY	 17
3.1 Fabrication of T-Gate Structures for GaN Field-Effect Transistors	17
3.2 Controlled Contamination of Optics under 157-nm Laser Irradiation	20
 4. BIOSENSOR AND MOLECULAR TECHNOLOGIES	 27
4.1 Effects of Flow-Cell Geometry and Lateral-Velocity Fields on Antigen Delivery in Microfluidic Channels	27
 5. ADVANCED IMAGING TECHNOLOGY	 31
5.1 Development of Low-Dark-Current Back-Illuminated Photodiodes	31

6.	ANALOG DEVICE TECHNOLOGY	37
6.1	Demonstration of Accurate Compensated Normal-Metal Chirp Filters on Alumina Substrates	37
7.	ADVANCED SILICON TECHNOLOGY	43
7.1	Three-Dimensional Circuit Integration Technology for Multiproject Fabrication	43

## LIST OF ILLUSTRATIONS

Figure No.		Page
1-1	Illustration of gain-switched $\text{Cr}^{4+}$ :YAG laser. AR, antireflecting; HR, highly reflecting; R, reflecting; ROC, radius of curvature.	3
1-2	Oscilloscope trace of output of gain-switched $\text{Cr}^{4+}$ :YAG laser. The first, short pulse is residual 1.064- $\mu\text{m}$ pump light. The second, broader pulse is the eye-safe output of the $\text{Cr}^{4+}$ :YAG laser.	4
1-3	Output spectrum of gain-switched $\text{Cr}^{4+}$ :YAG laser.	5
2-1	Illustration of evanescent-wave tunneling transmission. A TE wave is shown in which the electric field is perpendicular to the plane of incidence (the page). In the case of a TM wave (not shown), the <b>H</b> field is perpendicular to the plane of incidence.	8
2-2	Comparison of experimental tunneling transmissivity with theory. Note that better agreement is obtained when the polarization effect is included.	10
2-3	Test sample for measurement of evanescent-wave tunneling. The sample is bonded GaP/GaP, which contains an independently measured etched recess.	11
2-4	Experimental setup for measurement of evanescent-wave tunneling. The setup allows accurate sample orientation and positioning, and the tunneling measurement can be carried out in regions with and without the etched recess.	12
2-5	Measured intensities of tunneled and reflected beams across a sample. Note that the tunneled beam is $\sim 3$ times that of the reflected beam in the bonded region, but reduces to 0.1 times in the recessed region, i.e., region of a larger air gap.	13
3-1	Process flow for fabrication of T-gate: (a) application of resist layers and e-beam exposure, (b) development and plasma etch steps, (c) metal deposition, and (d) T-gate remaining after lift-off.	18
3-2	Electron micrographs of (a) resist profile and (b) completed T-gate.	19
3-3	Overall view of controlled contamination system, including gas delivery manifold and laser irradiation system.	21
3-4	Detailed view of controlled contamination cell containing optics under study.	21

## LIST OF ILLUSTRATIONS (Continued)

Figure No.		Page
3-5	Typical controlled contamination experiment for 5 ppm of toluene, showing (a) absence of contamination without laser light but with contaminant flowing over the optics, (b) transmission degradation of optics once the laser light is turned on, and (c) cleanup of the contaminated optics with laser light once the flow of contaminant is disabled.	23
3-6	Prediction of impact of contamination on an optical system for increasing number of optical surfaces. For a given number of optical surfaces, the expected normalized 157-nm transmission is shown by a hatched range, the uncertainty arising from an extrapolation of experimental data over several orders of magnitude of gas phase contaminant concentration. The gas phase contaminant concentration is 100 ppt. The total laser dose corresponds to one month of operation in a production environment: $10^9$ pulses at $0.1 \text{ mJ/cm}^2/\text{pulse}$ .	24
4-1	(a) An initial pulse of antigen reaches the post at early times. (b) At later times, antigen settles out in a concentrated zone in front of the post. Flow is from left to right. Note difference in color scales.	28
4-2	Surface binding for various flow-chamber geometries.	29
4-3	Effects of lateral velocity on surface concentration.	30
5-1	(a) Cross section of proposed photodiode geometry. $S$ is the lateral $p^+n$ junction channel-stop separation distance. (b) Calculation of dark current as a function of $S$ ( $\mu\text{m}$ ) based on an empirical model for the surface and bulk generation contributions to the diode leakage current for three different junction diameters.	32
5-2	Measured dark current of single interior diode as a function of reverse (applied to the substrate) bias. The measured diode is surrounded by an array of diodes that are biased at the voltage (with respect to the measured diode) indicated in the figure.	34
5-3	Measured dark current of identical geometry diodes for four different wafers, three back-illuminated wafers (50–100 $\mu\text{m}$ thick) and one full-thickness wafer. Surrounding "guard" diodes were biased at the same voltage as the measured diode.	35

## LIST OF ILLUSTRATIONS (Continued)

Figure No.		Page
6-1	(a) Layout and operation of proximity-tapped electromagnetic chirp filter. The filter is shown here as flat weighted and configured as a downchirp filter with the upchirp ports terminated into 50- $\Omega$ loads. The electromagnetic delay lines are implemented in stripline, and a cascade of backward-wave couplers implements the taps. (b) Tap strength can be increased to compensate for normal-metal (gold) conductor propagation loss. The requirement of weak coupling for all taps to avoid distorting the input signal sets a limit on the amount of compensation.	38
6-2	Frequency response of 2-GHz-bandwidth 16-ns-long Hamming-weighted gold-on-alumina chirp filter: (a) transmission ( $S_{21}$ ) vs frequency and (b) group delay vs frequency, both measured using the (compensated) downchirp ports of the filter. Measured data is shown along with the theoretical response. Note the linear downchirp group delay vs frequency characteristic. A curve also shows the theoretical transmission vs frequency response for an uncompensated filter.	39
6-3	Measured compressed-pulse response of linear microwave upchirp generator and normal-metal downchirp filter combination. An input signal at 11.6 GHz resulted in this chirp-transform output. The far-out error sidelobes are more than ~42 dB down from the mainlobe peak.	41
7-1	(a) Diagram of bonded analog-to-digital (A/D) (top) and imager integrated circuit layers, and (b) scanning electron micrograph cross section of a deep via.	44
7-2	Resistances of shallow and deep via chains.	45
7-3	Layout of A/D layer of three-dimensional (3D) ring oscillator, showing the pads used to connect the two active layers with 3D vias.	46
7-4	Delay per stage of 2D and 3D ring oscillators. The dimensions in the figure are the deep 3D via sizes.	47
7-5	Images obtained from $64 \times 64$ active pixel sensor with (a) normal and (b) near-infrared illumination. The photodiode signals generated in the imager layer are connected to asynchronous current-controlled relaxation oscillators in the A/D layer by 6- $\mu\text{m}$ deep 3D vias.	47

## LIST OF TABLES

Table No.		Page
2-1	Determination of Air Gap Between Tightly Bonded GaP/GaP	14
2-2	Test of Theory	14

## INTRODUCTION

### 1. QUANTUM ELECTRONICS

Miniature gain-switched  $\text{Cr}^{4+}$ :YAG lasers, pumped by passively  $Q$ -switched microchip lasers, provide a robust source of nanosecond pulses at eye-safe wavelengths, with potential applications in ranging and imaging. Similar devices can be developed to operate at diverse wavelengths from the ultraviolet to the mid infrared.

### 2. ELECTRO-OPTICAL MATERIALS AND DEVICES

Evanescent-wave tunneling transmission of visible light ( $\lambda = 633 \text{ nm}$ ) has been measured for etched air gaps of 20–80 nm and shown good agreement with the predictions of the electromagnetic theory. The narrow air gap between the tightly bonded GaP/GaP was then measured to be 1.3 nm.

### 3. SUBMICROMETER TECHNOLOGY

The fabrication of T-gate structures, to be used for GaN field-effect transistors, has been demonstrated using electron beam lithography. The method used for the fabrication was quickly developed and offers good robustness and flexibility.

Experiments have been performed to understand the impact of gas phase contamination on transmission of optics under 157-nm laser irradiation. Extrapolations to realistic contaminant levels and laser exposure doses were made to assess the impact of contamination on production optical systems.

### 4. BIOSENSOR AND MOLECULAR TECHNOLOGIES

Simple modifications of the flow-cell geometry and the introduction of lateral-velocity fields both can enhance the interaction of incoming particles with channel side walls by orders of magnitude. Such effects can be important in the design of devices with microfluidic components.

### 5. ADVANCED IMAGING TECHNOLOGY

Initial results have been obtained on the development of back-illuminated (BI) low-dark-current  $p^+$ -on- $n$  photodiodes fabricated on high-resistivity ( $>3000 \text{ } \Omega \text{ cm}$ ,  $n$ -type) Si substrates. Our BI diodes have demonstrated dark currents at least comparable to those obtained using a front-illuminated process, which is primarily the result of using a shallow phosphorus implant and furnace oxidation-anneal for the BI-side  $n^+$  region.

## **6. ANALOG DEVICE TECHNOLOGY**

Accurate 2-GHz-bandwidth 16-ns-long normal-metal (gold) chirp filters have been demonstrated by properly compensating for conductor propagation loss in the design. These filters have been used with a linear microwave chirp generator to produce compressed pulses with error sidelobes down by approximately 42 dB from the mainlobe peak.

## **7. ADVANCED SILICON TECHNOLOGY**

Three-dimensional silicon integrated circuits have been fabricated. The circuits are constructed by stacking of finished silicon-on-insulator wafers, removing one of the supporting silicon substrates, and forming vias through one of the circuits for electrical connection.

## REPORTS ON SOLID STATE RESEARCH

1 MAY THROUGH 31 JULY 2000

### PUBLICATIONS

- |   |   |  |
|---|---|--|
| Laser Cleaning of Optical Elements<br>in 157-nm Lithography                         | T. M. Bloomstein<br>M. Rothschild<br>V. Liberman<br>D. Hardy<br>N. N. Efremow, Jr.<br>S. T. Palmacci  | <i>Proc. SPIE</i> <b>4000</b> , 1537<br>(2000)   |
| New Materials for 157-nm<br>Photoresists: Characterization<br>and Properties        | M. K. Crawford*<br>A. E. Feiring*<br>J. Feldman*<br>R. H. French*<br>M. Periyasamy*<br>F. L. Schadt III*<br>R. J. Smalley*<br>F. C. Zumsteg*<br>R. R. Kunz<br>V. Rao*<br>L. Liao<br>S. M. Holl* | <i>Proc. SPIE</i> <b>3999</b> , 357<br>(2000)    |
| Temperature Dependence of Spin-<br>Lattice Relaxation in Rare-Earth<br>Iron Garnets | G. F. Dionne<br>G. L. Fitch   | <i>J. Appl. Phys.</i> <b>87</b> , 4963<br>(2000) |
| Encapsulated Inorganic Resist<br>Technology   | T. H. Fedynyshyn<br>S. P. Doran<br>M. L. Lind<br>I. Sondi*<br>E. Matijevich*  | <i>Proc. SPIE</i> <b>3999</b> , 627<br>(2000)    |

---

\*Author not at Lincoln Laboratory.

Prospects for Using Existing  
Resists for Evaluating 157-nm  
Imaging Systems

T. H. Fedynyshyn  
R. R. Kunz  
S. P. Doran  
R. B. Goodman  
M. L. Lind  
J. E. Curtin

*Proc. SPIE* **3999**, 335  
(2000)

Chromeless Phase-Shift Masks  
Used for Sub-100 nm SOI CMOS  
Transistors

M. Fritze  
D. K. Astolfi  
D. W. Yost  
P. W. Wyatt  
H-W. Liu  
A. R. Forte  
P. V. Davis  
A. V. Curtis  
D. M. Preble  
S. G. Cann

*Solid State Technol.* **43**, 116  
(2000)

Application of Chromeless Phase-  
Shift Masks to Sub-100 nm SOI  
CMOS Transistor Fabrication

M. Fritze  
J. A. Burns  
P. W. Wyatt  
D. K. Astolfi  
A. R. Forte  
D. K. Yost  
P. V. Davis  
A. V. Curtis  
D. M. Preble  
S. G. Cann  
S. J. Deneault  
H. Y. Liu\*  
J. C. Shaw\*  
N. T. Sullivan\*  
R. Brandon\*  
M. Mastovich\*

*Proc. SPIE* **4000**, 388  
(2000)

Optical Materials and Detector  
Characterization for VUV  
Lithography

R. Gupta\*  
J. Burnett\*  
V. Liberman

*Future Fab Int.* **9**, 161  
(2000)

---

\*Author not at Lincoln Laboratory.

Experimentation and Modeling of Organic Photocontamination on Lithographic Optics	R. R. Kunz V. Liberman D. K. Downs	<i>J. Vac. Sci. Technol. B</i> <b>18</b> , 1306 (2000); <i>Proc. SPIE</i> <b>4000</b> , 474 (2000)
Semiconductor Wafer Bonding via Liquid Capillarity	Z. L. Liao	<i>Appl. Phys. Lett.</i> <b>77</b> , 651 (2000)
Determination of Optical Properties of Thin Films and Surfaces in 157-nm Lithography	V. Liberman T. M. Bloomstein M. Rothschild	<i>Proc. SPIE</i> <b>3998</b> , 480 (2000)
Long-Term Testing of Optical Components for 157-nm Lithography	V. Liberman M. Rothschild J. H. C. Sedlacek R. S. Uttaro A. K. Bates* K. Orvek*	<i>Proc. SPIE</i> <b>4000</b> , 488 (2000)
Ultraviolet Photon Counting with GaN Avalanche Photodiodes	K. A. McIntosh R. J. Molnar L. J. Mahoney K. M. Molvar N. Efremow	<i>Appl. Phys. Lett.</i> <b>76</b> , 3938 (2000)
Resists and Other Critical Issues in 157-nm Lithography	M. Rothschild T. M. Bloomstein T. H. Fedynyshyn R. R. Kunz V. Liberman M. Switkes	<i>J. Photopolym. Sci. Technol.</i> <b>13</b> , 369 (2000)
Interference Lithography at 157 nm	M. Switkes T. M. Bloomstein M. Rothschild	<i>Proc. SPIE</i> <b>4000</b> , 1590 (2000)

---

\*Author not at Lincoln Laboratory.

Comparison of Power Dependence  
of Microwave Surface Resistance of  
Unpatterned and Patterned YBCO  
Thin Film

H. Xin  
D. E. Oates  
A. C. Anderson  
R. L. Slattery  
G. Dresselhaus\*  
M. S. Dresselhaus\*

*IEEE Trans. Microw. Theory  
Tech.* **48**, 1221 (2000)

Observation of Individual  
Josephson Vortices in  
YBa<sub>2</sub>Cu<sub>3</sub>O<sub>7- $\delta$</sub>  Bicrystal  
Grain-Boundary Junction

H. Xin  
D. E. Oates  
S. Sridhar\*  
G. Dresselhaus\*  
M. S. Dresselhaus\*

*Phys. Rev. B, Condens. Matter*  
**61**, R14 952 (2000)

Passively Q-Switched Nd:YAG  
Microchip Lasers and Applications

J. J. Zayhowski

*J. Alloys Compounds*  
**303-304**, 393 (2000)

#### ACCEPTED FOR PUBLICATION

All-Active InGaAsP/InP Optical  
Tapered-Amplifier  $1 \times N$  Power  
Splitters

J. P. Donnelly  
R. E. Reeder  
R. J. Bailey  
P. J. Taylor  
A. Napoleone  
W. D. Goodhue  
S. S. Choi\*

*IEEE Photon. Technol. Lett.*

Accurate Modeling of Dual Dipole  
and Slot Elements Used with  
Photomixers for Coherent  
Terahertz Output Power

S. M. Duffy  
S. Verghese  
K. A. McIntosh  
A. Jackson\*  
A. C. Gossard\*  
S. Matsuura\*

*IEEE Trans. Microw. Theory  
Technol.*

UV And VUV Sources and  
Materials for Lithography

V. Liberman  
M. Rothschild

*Ultraviolet Spectrosc.*

---

\*Author not at Lincoln Laboratory.

High Spatial Resolution Thermal  
Conductivity and Raman  
Spectroscopy Investigation of  
Hydride Vapor Phase Epitaxy  
Grown *n*-GaN/Sapphire (0001):  
Doping Dependence

R. J. Molnar  
D. I. Florescu\*  
V. M. Asnin\*  
F. H. Pollak\*  
C. E. Wood\*

*J. Appl. Phys.*

Spectroscopy of Competing  
Mechanisms Generating  
Stimulated Emission in GaN

R. Molnar  
W. D. Herzog\*  
G. E. Bunea\*  
M. S. Unlü\*  
B. B. Goldberg\*

*Appl. Phys. Lett.*

Encapsulation of Nanosized Silica  
by In Situ Polymerization of t-Butyl  
Acrylate

I. Sondi\*  
T. H. Fedynyshyn  
R. Sinta\*  
E. Matijevich\*

*Langmuir*

GaN Avalanche Photodiode  
Operating in Linear-Gain Mode  
and Geiger Mode

S. Verghese  
K. A. McIntosh  
R. J. Molnar  
L. J. Mahoney  
K. Molvar  
R. L. Aggarwal

*IEEE Trans. Electron Devices*

Growth of Low Bandgap III-V  
Alloys for Mid-Infrared Devices

C. A. Wang

*In Encyclopedia of Materials  
Science and Technology*  
(Elsevier Science, Oxford,  
England)

Diode-Pumped 214.8-nm Nd:YAG/  
Cr<sup>4+</sup>:YAG Microchip Laser  
System for the Detection of NO

J. Wormhoudt\*  
J. H. Shorter\*  
J. J. Zayhowski  
C. C. Cook

*Appl. Opt.*

---

\*Author not at Lincoln Laboratory.

Passively *Q*-Switched 214.8-nm  
Nd:YAG/Cr<sup>4+</sup>:YAG Microchip  
Laser System for the Detection of  
NO

J. J. Zayhowski  
C. C. Cook  
J. Wormhoudt\*  
J. Shorter\*

*Trends in Optics and Photonics  
Series*

Miniature Sources of  
Subnanosecond 1.4–4.3- $\mu$ m  
Pulses with High Peak Power

J. J. Zayhowski  
A. L. Wilson

*Trends in Optics and Photonics  
Series*

### PRESENTATIONS<sup>†</sup>

High-Power Optically Pumped  
GaInSb/InAs Quantum-Well Lasers  
with GaInAsSb Integrated Absorber  
Layers Emitting at 4  $\mu$ m

H. K. Choi  
A. K. Goyal  
P. J. Foti  
S. C. Buchter  
G. W. Turner  
M. J. Manfra  
S. Calawa

2000 Conference on Lasers and  
Electro-Optics,  
San Francisco, California,  
7-12 May 2000

Spectral Beam Combining of a  
Broad-Stripe Diode Laser Array in  
an External Cavity

V. Daneu  
A. Sanchez  
T. Y. Fan  
H. K. Choi  
G. W. Turner  
C. C. Cook

2000 Conference on Lasers and  
Electro-Optics,  
San Francisco, California,  
7-12 May 2000

Measurement of Mode-Locked  
Laser Timing Jitter Using Phase-  
Encoded Optical Sampling

P. W. Juodawlkis  
J. L. Wasserman  
J. J. Hargreaves  
R. C. Williamson  
J. C. Twichell

2000 Conference on Lasers and  
Electro-Optics,  
San Francisco, California,  
7-12 May 2000

---

\*Author not at Lincoln Laboratory.

<sup>†</sup> Titles of presentations are listed for information only. No copies are available for distribution.

High- $Q$ Silicon-Based Microring Resonators Fabricated Using Optical Lithography	P. A. Maki M. Fritze	2000 Conference on Lasers and Electro-Optics, San Francisco, California, 7-12 May 2000
Photogenerated Carrier Dynamics in GaN	R. J. Molnar G. E. Bunea* G. Ulu* M. S. Unlü* B. B. Goldberg*	2000 Conference on Lasers and Electro-Optics, San Francisco, California, 7-12 May 2000
Extending the Performance of Optically Sampled Time-Demultiplexed Analog-to-Digital Converters	J. C. Twichell P. W. Juodawlkis J. L. Wasserman R. C. Williamson G. E. Betts	2000 Conference on Lasers and Electro-Optics, San Francisco, California, 7-12 May 2000
Effects of Crosstalk in Demultiplexed Photonic A/D Converters	R. C. Williamson P. W. Juodawlkis J. L. Wasserman G. E. Betts J. C. Twichell	2000 Conference on Lasers and Electro-Optics, San Francisco, California, 7-12 May 2000
Nanofabrication Potential of Resolution-Enhanced Optical Lithography Sample	M. Fritze	DARPA Workshop for Applied Physics of Nanostructures and Nanoscale Materials, Washington, D. C., 8 May 2000
Performance Evaluation of 157-nm Optical Materials	A. K. Bates* V. Liberman M. Rothschild J. H. C. Sedlacek R. S. Uttaro C. VanPeski* R. Gupta* J. Burnett* M. Dowel* S. E. Gianoulakis*	International Symposium on 157 nm Lithography, Dana Point, California, 8-11 May 2000

---

\*Author not at Lincoln Laboratory.

Laser Surface Cleaning of Optical Elements in 157-nm Lithography	T. M. Bloomstein M. Rothschild V. Liberman D. Hardy N. N. Efremow S. T. Palmacci	International Symposium on 157 nm Lithography, Dana Point, California, 8-11 May 2000
Polymer Photochemistry at the 157-nm Wavelengths	T. H. Fedynyshyn R. R. Kunz R. Sinta R. B. Goodman S. P. Doran	International Symposium on 157 nm Lithography, Dana Point, California, 8-11 May 2000
Photo-induced Outgassing Candidates for 157-nm Resist Materials	R. R. Kunz D. K. Downs T. H. Fedynyshyn R. Sinta M. Sworin	International Symposium on 157 nm Lithography, Dana Point, California, 8-11 May 2000
Controlled Contamination of Optics Under 157-nm Laser Irradiation	V. Liberman T. M. Bloomstein M. Rothschild	International Symposium on 157 nm Lithography, Dana Point, California, 8-11 May 2000
Determination of Optical Properties of Thin Films and Surfaces in 157-nm Lithography	V. Liberman T. M. Bloomstein M. Rothschild	International Symposium on 157 nm Lithography, Dana Point, California, 8-11 May 2000
Can Secondary Optical Materials Help Enable Refractive Lenses for 157-nm Lithography?	K. Orvek* V. Liberman M. Rothschild J. H. C. Sedlacek R. S. Uttaro	International Symposium on 157 nm Lithography, Dana Point, California, 8-11 May 2000
Materials Issues in 157-nm Photomasks	M. Rothschild V. Liberman J. H. C. Sedlacek R. S. Uttaro	International Symposium on 157 nm Lithography, Dana Point, California, 8-11 May 2000

---

\*Author not at Lincoln Laboratory.

Patterning of Dense Sub-50-nm  
Features with 157-nm Interference  
Lithography

M. Switkes  
T. M. Bloomstein  
M. Rothschild

International Symposium on  
157 nm Lithography,  
Dana Point, California,  
8-11 May 2000

The Growth and Characterization of  
InGaAsP/InP Materials for High-  
Power Optical Devices

P. J. Taylor  
J. P. Donnelly  
J. N. Walpole  
R. J. Bailey  
L. J. Missaggia  
D. R. Calawa

12th International Conference  
on Indium Phosphide and  
Related Materials,  
Williamsburg, Virginia,  
14-18 May 2000

Optical Sampling for Analog-to-  
Digital Conversion

J. C. Twichell

Lincoln Laboratory  
Technical Seminar Series,  
University of California,  
Los Angeles, California,  
19 May 2000

Polymer Photochemistry at  
Advanced Optical Wavelengths

T. H. Fedynyshyn  
R. R. Kunz  
R. Sinta  
R. B. Goodman  
S. P. Doran

44th International Conference  
on Electron, Ion and Photon  
Beam Technology and  
Nanofabrication,  
Rancho Mirage, California,  
30 May–2 June 2000

Sub-100 nm SOI CMOS by DUV  
Optical Lithography

M. Fritze  
J. Burns  
C. K. Chen  
C-L. Chen

44th International Conference  
on Electron, Ion and Photon  
Beam Technology and  
Nanofabrication,  
Rancho Mirage, California,  
30 May–2 June 2000

Nanostructured Thermoelectric  
Materials and Devices

T. C. Harman  
P. J. Taylor  
M. P. Walsh

DARPA/ONR Thermoelectrics  
Principal Investigators Meeting,  
Hilton Head, South Carolina,  
31 May–2 June 2000

Advances in Optical Converter  
Architectures

J. C. Twichell  
P. W. Juodawlkis  
J. L. Wasserman  
G. E. Betts  
R. C. Williamson

Defense Science Research  
Council Workshop,  
Washington, D.C.,  
2 June 2000

Sub-100 nm SOI CMOS by 248 nm  
Optical Lithography

M. Fritze

Advanced Reticle Symposium,  
San Jose, California,  
3 June 2000

Laser Beam Combining of Fiber  
and Diode Laser Arrays for Power  
and Brightness Scaling

T. Y. Fan  
A. Sanchez  
V. Daneu  
A. Goyal  
R. L. Aggarwal  
S. C. Buchter  
H. K. Choi  
G. W. Turner  
C. C. Cook

2000 Diode Laser Technology  
Review,  
Albuquerque, New Mexico,  
5-8 June 2000

Multi-spectral Semiconductor  
Laser System for Infrared  
Countermeasures

A. K. Goyal  
J. Ochoa  
V. Daneu  
S. C. Buchter  
G. W. Turner  
H. K. Choi  
J. Walpole  
Z. L. Liao  
P. J. Foti  
M. J. Manfra  
T. Y. Fan  
A. Sanchez

2000 Diode Laser Technology  
Review,  
Albuquerque, New Mexico,  
5-8 June 2000

MEMS Microswitch Arrays for  
Reconfigurable Distributed  
Microwave Components

C. O. Bozler  
R. G. Drangmeister\*  
S. M. Duffy  
M. A. Gouker  
J. M. Knecht  
L. J. Kushner  
R. J. Parr  
S. Rabe  
L. Travis

International Microwave  
Symposium,  
Boston, Massachusetts,  
11-16 June 2000

Status of 157-nm Lithography

M. Rothschild

IBM Lithography Symposium,  
Burlington, Vermont,  
12 June 2000

Ultraviolet Photon Counting with  
GaN Avalanche Photodiodes

K. A. McIntosh  
S. Verghese  
R. J. Molnar  
L. J. Mahoney  
K. M. Molvar  
R. L. Aggarwal  
I. L. Melngailis

Device Research  
Conference,  
Denver, Colorado,  
19-21 June 2000

High Spatial Resolution Thermal  
Conductivity and Raman  
Spectroscopy Investigation of  
Hydride Vapor Phase Epitaxy  
Grown *n*-GaN/Sapphire (0001):  
Doping Dependence

R. J. Molnar  
D. I. Florescu\*  
V. M. Asnin\*  
F. H. Pollak\*  
C. E. C. Wood\*

42nd Electronic Materials  
Conference,  
Denver, Colorado,  
21-23 June 2000

THz Applications for Low-  
Temperature-Grown GaAs

S. Verghese

NATO Advanced Research  
Workshop,  
Toulouse, France,  
21-28 June 2000

Metallo-dielectric Photonic Crystal  
Design for Infrared Applications

S. Verghese  
K. A. McIntosh  
J. A. Oswald  
B.-I. Wu

Progress in Electromagnetics  
Research Symposium,  
Cambridge, Massachusetts,  
5-14 July 2000

---

\*Author not at Lincoln Laboratory.

In Situ Raman Spectroscopic  
Characterization of Compound  
Semiconductor Free Carrier  
Concentration

C. A. Wang  
D. C. Oakley  
J. E. Maslar\*

2000 IEEE/LEOS Summer  
Topical Meeting on Optical  
Sensing in Semiconductor  
Manufacturing,  
Aventura, Florida,  
24-26 July 2000

---

\*Author not at Lincoln Laboratory.

## ORGANIZATION

### SOLID STATE DIVISION

D. C. Shaver, *Head*  
R. W. Ralston, *Associate Head*  
N. L. DeMeo, Jr., *Assistant*  
Z. J. Lemnios, *Senior Staff*

J. W. Caunt, *Assistant Staff*  
K. J. Challberg, *Administrative Staff*  
J. D. Pendergast, *Administrative Staff*

### SUBMICROMETER TECHNOLOGY

M. Rothschild, *Leader*  
T. M. Lyszcza, *Assistant Leader*  
T. H. Fedynyshyn, *Senior Staff*  
R. R. Kunz, *Senior Staff*

Astolfi, D. K.  
Bloomstein, T. M.  
DiNatale, W. F.  
Doran, S. P.  
Efremow, N. N., Jr.  
Forte, A. R.  
Geis, M. W.  
Goodman, R. B.  
Krohn, K. E.

Liberman, V.  
Maki, P. A.  
Palmacci, S. T.  
Sedlacek, J. H. C.  
Spector, S. J.  
Switkes, M.  
Sworin, M.  
Uttaro, R. S.

### QUANTUM ELECTRONICS

A. Sanchez-Rubio, *Leader*  
T. Y. Fan, *Assistant Leader*  
T. H. Jeys, *Senior Staff*  
J. J. Zayhowski, *Senior Staff*

Aggarwal, R. L.  
Buchter, S. C.  
Daneu, J. L.  
Daneu, V.  
DiCecca, S.

Goyal, A. K.  
Herzog, W. D.  
Lynch, E. J.  
O'Brien, P. W.  
Ochoa, J. R.

### ELECTRO-OPTICAL MATERIALS AND DEVICES

J. C. Twichell, *Leader*  
D. L. Spears, *Assistant Leader\**  
G. W. Turner, *Assistant Leader*  
H. K. Choi, *Senior Staff*  
R. C. Williamson, *Senior Staff*

Bailey, R. J.  
Betts, G. E.  
Calawa, A. R.\*  
Calawa, D. R.  
Calawa, S. D.  
Connors, M. K.  
Donnelly, J. P.  
Goodhue, W. D.  
Hargreaves, J. J.  
Harman, T. C.

Harris, C. T.  
Juodawlkis, P. W.  
Liau, Z. L.  
Mahoney, L. J.  
Manfra, M. J.  
McIntosh, K. A.  
Missaggia, L. J.  
Molnar, R. J.  
Mull, D. E.  
Napoleone, A.

Nitishin, P. M.  
Oakley, D. C.  
O'Donnell, F. J.  
Poillucci, R. J.  
Taylor, P. J.  
Verghese, S.  
Walpole, J. N.  
Wang, C. A.  
Wasserman, J. L.  
Younger, R. D.

---

\*Part Time

BIOSENSOR AND MOLECULAR  
TECHNOLOGIES

M. A. Hollis, *Leader*

Blanchard, D. J.	Parameswaran, L.
Graves, C. A.	Petrovick, M. S.
Harper, J. D.	Rider, T. H.
Mathews, R. H.	Young, A. M.
Nargi, F. E.	

ANALOG DEVICE TECHNOLOGY

T. C. L. G. Sollner, *Leader*  
L. M. Johnson, *Assistant Leader*  
A. C. Anderson, *Senior Staff*

Anthony, M. P.	Murphy, P. G.
Berggren, K. K.	Oates, D. E.
Boisvert, R. R.	Sage, J. P.
Feld, D. A.	Santiago, D. D.
Fitch, G. L.	Seaver, M. M.
Holtham, J. H.	Slattery, R. L.
Kohler, E. J.	Weir, T. J.
Lyons, W. G.	Whittington, R. H.
Macedo, E. M., Jr.	

ADVANCED IMAGING TECHNOLOGY

B. B. Kosicki, *Leader*  
R. K. Reich, *Assistant Leader*  
B. E. Burke, *Senior Staff*

Aull, B. F.	Lind, T. A.
Cooper, M. J.	Loomis, A. H.
Craig, D. M.	McGonagle, W. H.
Daniels, P. J.	O'Mara, D. M.
Doherty, C. L., Jr.	Percival, K. A.
Dolat, V. S.	Rathman, D. D.
Felton, B. J.	Stern, A.
Gregory, J. A.	Young, D. J.
Johnson, K. F.	

ADVANCED SILICON TECHNOLOGY

C. L. Keast, *Leader*  
P. W. Wyatt, *Associate Leader*

Austin, E. E.	Knecht, J. M.
Berger, R.	Newcomb, K. L.
Bozler, C. O.	Rabe, S.
Burns, J. A.	Soares, A. M.
Chen, C. K.	Suntharalingam, V.
Chen, C. L.	Travis, L.
Davis, P. V.	Tyrrell, B. M.
D'Onofrio, R. P.	Warner, K.
Fritze, M.	Yost, D.-R.
Gouker, P. M.	Young, G. R.

# 1. QUANTUM ELECTRONICS

## 1.1 MINIATURE EYE-SAFE GAIN-SWITCHED LASER FOR RANGING APPLICATIONS

Passively  $Q$ -switched microchip lasers are attractive sources for high-precision ranging because of their short pulse duration and excellent pulse stability, combined with their simplicity, small size, robustness, and low cost [1]–[4]. For many ranging applications it is desirable to have a source that operates in the eye-safe spectral region near  $1.5\ \mu\text{m}$ . Although passively  $Q$ -switched microchip lasers have been developed to operate in this wavelength region [5],[6], the saturable absorbers and/or gain media lack some of the desirable material properties that are intrinsic to  $1\text{-}\mu\text{m}$  Nd:YAG/Cr<sup>4+</sup>:YAG systems. There is ongoing work to generate eye-safe sources using optical parametric devices pumped by  $1\text{-}\mu\text{m}$  microchip lasers [7]–[9]. This approach, however, sacrifices some of the simplicity, robustness, and cost advantage inherent with the passively  $Q$ -switched microchip laser. Miniature eye-safe gain-switched lasers, pumped by passively  $Q$ -switched  $1\text{-}\mu\text{m}$  microchip lasers, maintain the advantages of the passively  $Q$ -switched  $1\text{-}\mu\text{m}$  microchip laser while operating at the desired eye-safe wavelength.

The shortest pulse that can be obtained from a gain-switched laser is [10]

$$t_w = \frac{8.1t_{rt}}{\ln(G_{rt})} \quad (1.1)$$

where  $t_w$  is the full width at half-maximum of the output pulse,  $t_{rt}$  is the round-trip time of light within the laser cavity, and  $G_{rt}$  is the small-signal round-trip gain of the cavity at the time the pulse forms. For a monolithic laser,

$$t_{rt} = \frac{2nl}{c} \quad (1.2)$$

where  $n$  is the refractive index of the material in the cavity,  $l$  is the cavity length, and  $c$  is the speed of light in vacuum. The small-signal round-trip gain is given by

$$G_{rt} = \exp(2n_i\sigma_{\text{eff}}l) \quad (1.3)$$

where  $n_i$  is the inversion density averaged over the volume of the oscillating mode and  $\sigma_{\text{eff}}$  is the effective gain cross section of an inverted ion. The shortest pulse that can be obtained for a given gain medium is, therefore,

$$t_w = \frac{8.1n}{cn_i\sigma_{\text{eff}}} \quad (1.4)$$

The maximum energy that can be extracted in an output pulse is

$$E_p = \zeta V n_i h \frac{c}{\lambda} \quad (1.5)$$

where  $\zeta$  is the extraction efficiency of the output pulse,  $V$  is the volume of the oscillating mode in the gain medium,  $h$  is Planck's constant, and  $\lambda$  is the (free-space) wavelength of oscillation.

One attractive gain medium for a robust eye-safe gain-switched laser is  $\text{Cr}^{4+}$ :YAG, the same material that is used to  $Q$  switch the passively  $Q$ -switched 1- $\mu\text{m}$  microchip laser. The large absorption cross section of the  $\text{Cr}^{4+}$  ions in YAG at 1.064  $\mu\text{m}$  results in a saturation fluence that is much less than the fluence obtained directly from the passively  $Q$ -switched microchip laser. (The saturation fluence for  $\text{Cr}^{4+}$ :YAG at 1.064  $\mu\text{m}$  is  $\sim 16 \text{ mJ/cm}^2$ ; the fluence exiting the 1.064- $\mu\text{m}$  microchip laser can be 10–100 times greater [3].) As a result, the 1.064- $\mu\text{m}$  light bleaches the absorption at that wavelength, efficiently inverting the transition near 1.5  $\mu\text{m}$ . The length of the  $\text{Cr}^{4+}$ :YAG can be chosen so that the 1.064- $\mu\text{m}$  absorption is bleached along the entire length while absorbing most of the 1.064- $\mu\text{m}$  pump energy.

For high-concentration  $\text{Cr}^{4+}$ :YAG, with an absorption coefficient of  $6 \text{ cm}^{-1}$ , the maximum possible inversion density is  $n_i \approx 10^{18} \text{ cm}^{-3}$ . The peak effective gain cross section at 1.42  $\mu\text{m}$  is  $\sigma_{\text{eff}} \approx 1.7 \times 10^{-19} \text{ cm}^2$  ( $\sigma_{\text{eff}} = \sigma_g - \sigma_{\text{ESA}}$ , where  $\sigma_g$  is the true gain cross section and  $\sigma_{\text{ESA}}$  is the cross section for excited-state absorption) [11],[12] and the refractive index  $n = 1.82$ . The shortest obtainable pulse width is, therefore,  $t_w = 2.9 \text{ ns}$ . The maximum extraction efficiency  $\zeta$  that can be obtained in  $\text{Cr}^{4+}$ :YAG is limited by excited-state absorption to about 0.4 ( $\zeta_{\text{max}} = \sigma_{\text{eff}}/\sigma_g$ ) [13].

To demonstrate the concepts described above, a  $\text{Cr}^{4+}$ :YAG laser was constructed from a 7-mm-long piece of  $\text{Cr}^{4+}$ :YAG and a separate output coupler, as illustrated in Figure 1-1. The  $\text{Cr}^{4+}$ :YAG had an unsaturated absorption coefficient of  $6 \text{ cm}^{-1}$  at 1.064  $\mu\text{m}$  and was polished to have two flat and parallel faces. One face (the input face) was coated to be highly transmitting at the pump wavelength of 1.064  $\mu\text{m}$  and highly reflecting at the oscillating wavelength, 1.45  $\mu\text{m}$ . There was 2% transmission through the input coating at 1.45  $\mu\text{m}$ , representing a parasitic loss to the system. The opposite face was antireflection coated at 1.45  $\mu\text{m}$ . The output coupler had a 1-cm radius of curvature and 5% transmission at the oscillating wavelength. The total length of the laser cavity was 1 cm. The laser was longitudinally pumped with the 80- $\mu\text{J}$  output of a high-power microchip laser. The pulse length of the pump laser was  $\sim 400 \text{ ps}$ ; the  $1/e^2$  radius of the pump spot was  $\sim 80 \mu\text{m}$ .

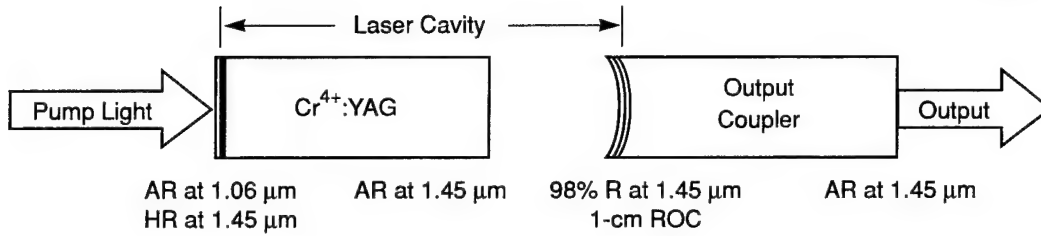


Figure 1-1. Illustration of gain-switched  $\text{Cr}^{4+}:\text{YAG}$  laser. AR, antireflecting; HR, highly reflecting; R, reflecting; ROC, radius of curvature.

The laser cavity was designed for experimental convenience, not optimal performance. Because of the way it was constructed, the minimum pulse width that could be expected was somewhat larger than the number given above (2.9 ns). The fact that the laser cavity is not monolithic increases the minimum possible pulse width by a factor of  $[l + l_{\text{YAG}}(n-1)]/nl_{\text{YAG}}$ , where  $l_{\text{YAG}}$  is the length of the  $\text{Cr}^{4+}:\text{YAG}$  crystal. The gain cross section at  $1.45 \mu\text{m}$  is about 25% lower than the gain cross section at  $1.42 \mu\text{m}$  [12], further increasing the pulse width by  $\sigma_g(1.42)/\sigma_g(1.45)$ . The net result is that the minimum theoretical pulse width for this cavity operating at  $1.45 \mu\text{m}$  is 4.8 ns.

The  $1/e^2$  mode waist  $\omega_0$  for the laser cavity is  $46 \mu\text{m}$ , located at the input face of the  $\text{Cr}^{4+}:\text{YAG}$ . The effective mode volume in the  $\text{Cr}^{4+}:\text{YAG}$ , out to the  $1/e^2$  mode waist, is  $V = \pi\omega_0^2 l_{\text{YAG}}(1 + l_{\text{YAG}}^2/3l_c^2)$ , where the confocal parameter  $l_c = \pi\omega_0^2 n/\lambda$ . The maximum pulse energy that can be extracted is  $3.3 \mu\text{J}$ . The minimum amount of absorbed pump energy required to totally invert the oscillating mode volume is  $12 \mu\text{J}$ , an energy level consistent with what can be obtained from low-power microchip lasers pumped with a 1.2-W diode laser [3].

The high-power microchip laser used to pump the  $\text{Cr}^{4+}:\text{YAG}$  laser produces a fluence of  $\sim 800 \text{ mJ}/\text{cm}^2$  throughout the laser's oscillating mode volume. This is 50 times the saturation fluence of the  $\text{Cr}^{4+}:\text{YAG}$ , and ensures nearly 100% inversion of the gain medium, consistent with the modeling performed above. By pumping a larger volume than required, alignment of the laser is simplified. Nearly total inversion of the gain medium and simplified alignment are achieved at the expense of system efficiency—no matter how hard the laser is pumped, the most energy that can be extracted in the fundamental transverse mode is  $\sim 3 \mu\text{J}$  per pulse, and that can be done with a much lower power pump. Optimization of the laser efficiency will be performed at a later time as applications for this technology evolve.

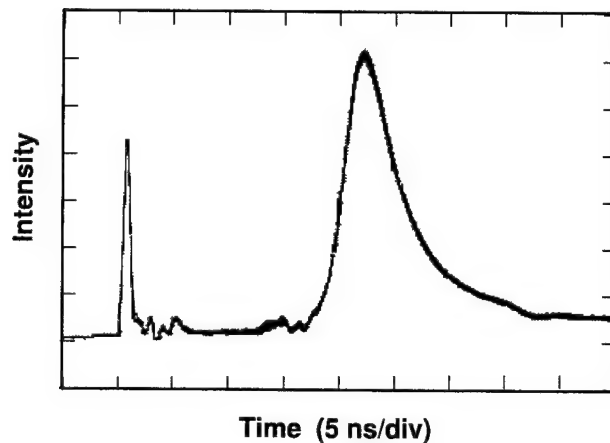


Figure 1-2. Oscilloscope trace of output of gain-switched  $\text{Cr}^{4+}:\text{YAG}$  laser. The first, short pulse is residual  $1.064\text{-}\mu\text{m}$  pump light. The second, broader pulse is the eye-safe output of the  $\text{Cr}^{4+}:\text{YAG}$  laser.

The performance of the laser was close to the predictions of the simple model outlined above. The laser produced a 6-ns output pulse with a pulse energy of  $2.0\text{ }\mu\text{J}$ , measured through the output coupler only. Once we include the energy transmitted through the input coupler, the total optical energy extracted from the gain medium is  $2.8\text{ }\mu\text{J}$ . The buildup time of the output pulse was  $\sim 21\text{ ns}$ , as shown in Figure 1-2. The far-field profile of the output indicated that the laser was oscillating in the fundamental transverse mode, and the amplitude of the pulse was stable to better than  $\pm 0.5\%$ .

The output spectrum of the gain-switched laser, shown in Figure 1-3, had a full width at half-maximum of  $\sim 25\text{ nm}$ , centered near  $1.44\text{ }\mu\text{m}$ . Although the trace shown in Figure 1-3 was obtained by averaging several thousand output pulses, it was confirmed that each individual pulse had a similar spectrum; the broad spectral profile is not the result of many different pulses operating at different frequencies. The width of the output spectrum is probably limited by the performance of the output coupler. For ranging and imaging applications, the broad spectrum eliminates the laser speckle that can plague narrowband systems.

The broad gain bandwidth of  $\text{Cr}^{4+}:\text{YAG}$  should allow this laser to be operated at any wavelength from  $\sim 1.3$  to  $1.6\text{ }\mu\text{m}$ , with the proper output coupler. Miniature gain-switched lasers can also be developed to access other regions of the spectrum, for a wide variety of applications. A gain-switched  $\text{Ti}:\text{Al}_2\text{O}_3$  laser pumped by the second harmonic of a passively  $Q$ -switched  $\text{Nd}:\text{YAG}$  microchip laser could operate at wavelengths throughout the near infrared, from  $\sim 0.65$  to  $1.1\text{ }\mu\text{m}$ ; a  $\text{Ce}^{3+}$ -doped fluoride laser pumped by the fourth harmonic of a passively  $Q$ -switched microchip laser could operate throughout portions of the

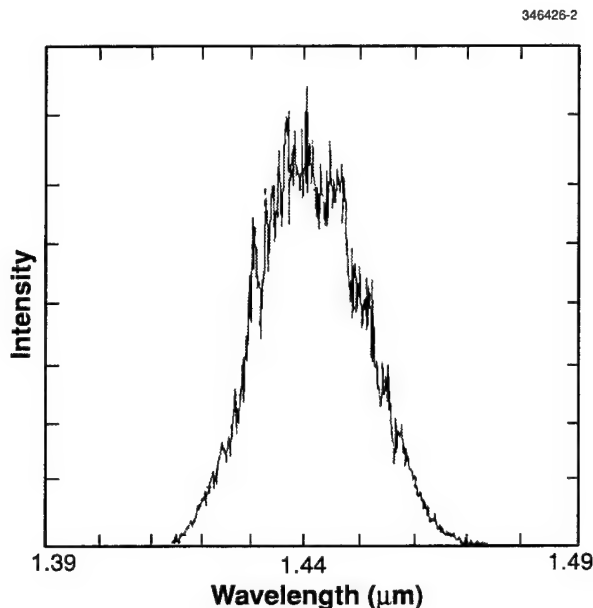


Figure 1-3. Output spectrum of gain-switched  $\text{Cr}^{4+}$ :YAG laser.

near ultraviolet, from ~280 to 320 nm [14]. Both of these laser systems have a much larger effective gain cross section than  $\text{Cr}^{4+}$ :YAG, giving them the potential for much shorter output pulses. Both will be further investigated in the near future.

When the gain-switched laser contains air space, or other elements in addition to the gain medium, the output pulses will be longer than in the case of a monolithic cavity since the round-trip time of light will increase without a commensurate increase in the round-trip gain. There may be cases, however, where it is desirable to include other elements in the cavity for transverse mode control or for frequency control and tunability. For example, with a broadband output coupler and an intracavity frequency selective element, a gain-switched laser could be actively tuned throughout its gain bandwidth. Alternatively, intracavity elements could be used to narrow the output spectrum, perhaps forcing single-mode operation. Another interesting example of a non-monolithic cavity is a single laser cavity that is both the passively  $Q$ -switched pump laser and the gain-switched laser [15].

Miniature gain-switched lasers, pumped by passively  $Q$ -switched microchip lasers, offer the potential for extremely compact and robust sources of laser radiation at diverse wavelengths. These systems will be developed to meet the requirements of applications as they emerge.

J. J. Zayhowski

## REFERENCES

1. J. J. Zayhowski, *Laser Focus World* **35** (August), 129 (1999).
2. J. J. Zayhowski, *J. Alloys Compounds* **303–304**, 393 (2000).
3. J. J. Zayhowski, *Rev. Laser Eng.* **26**, 841 (1998).
4. J. J. Zayhowski and C. Dill III, *Opt. Lett.* **19**, 1427 (1994).
5. P. Thony, B. Ferrand, and E. Molva, *OSA Trends in Optics and Photonics*, Vol. 19, *Advanced Solid State Lasers*, W. R. Bosenberg and M. M. Fejer, eds. (Optical Society of America, Washington, D.C., 2000), p. 150.
6. R. Fluck, R. Häring, R. Paschotta, E. Gini, H. Melchior, and U. Keller, *Appl. Phys. Lett.* **72**, 3273 (1998).
7. J. J. Zayhowski and A. L. Wilson, *OSA Trends in Optics and Photonics*, Vol. 34, *Advanced Solid State Lasers*, U. Keller, H. Injeyan, and C. Marshall, eds. (Optical Society of America, Washington, D.C., 2000), p. 308.
8. J. J. Zayhowski, *Opt. Lett.* **22**, 169 (1997).
9. L. Fulop, L. Fulbert, and E. Molva, *Conference on Lasers and Electro-Optics, 1998 Technical Digest Series*, Vol. 6 (Optical Society of America, Washington, D.C., 1998), p. 136.
10. J. J. Zayhowski and P. L. Kelley, *IEEE J. Quantum Electron.* **27**, 2220 (1991); **29**, 1239 (1993).
11. S. Küick, K. L. Schepler, K. Peterman, and G. Huber, *OSA Trends in Optics and Photonics*, Vol. 1, *Advanced Solid State Lasers*, S. A. Payne and C. Pollock, eds. (Optical Society of America, Washington, D.C., 1996), p. 94.
12. S. Küick, K. Peterman, and G. Huber, *OSA Proceedings on Advanced Solid State Lasers*, 1991, Vol. 10, G. Dubé and L. Chase, eds. (Optical Society of America, Washington, D.C., 1991), p. 92.
13. N. Borodin, V. Zhitnyuk, A. Okhrimchuk, and A. Shestakov, *Izv. Akad. Nauk SSSR, Ser. Fiz.* **54**, 1500 (1990).
14. C. D. Marshall, J. A. Speth, S. A. Payne, W. F. Krupke, G. J. Quarles, V. Castillo, and B. H. T. Chai, *J. Opt. Soc. Am. B* **11**, 2054 (1994).
15. K. Spariosu, W. Chen, R. Stultz, M. Birnbaum, and A. V. Shestakov, *Opt. Lett.* **18**, 814 (1993).

## 2. ELECTRO-OPTICAL MATERIALS AND DEVICES

### 2.1 MEASUREMENT OF NANOMETER AIR GAPS IN SEMICONDUCTOR WAFER BONDING

There has been considerable interest in wafer bonding [1]–[3] and wafer fusion [4]–[9] for integration of dissimilar semiconductor materials, devices, and systems. In wafer bonding, two clean surfaces are brought to close contact either by mechanical pressing [2] or by liquid surface tension [1],[3]. The wafer couples are then tightly held together by molecular force. The average distance between the two surfaces and the resulting bonding strength are of basic importance. However, for strong bonding, the gap needs to be close to the atomic distance and cannot be measured by optical interferometry. The bonded interfaces are also not easily accessible to sensitive electron-beam probing [1].

In this work, we describe a nondestructive optical technique utilizing the evanescent wave in total internal reflection. It is well known that when a second dielectric is brought to within the range of the evanescent field, some transmission occurs. Also known as frustrated total internal reflection, this phenomenon is a close analogy to quantum-mechanical tunneling, but its potential for sensitive quantitative measurement was never utilized. We first carry out a comprehensive theoretical treatment taking into consideration the vector nature of the electromagnetic field. The theory is then tested experimentally and used to measure the narrow air gap in wafer-bonded GaP/GaP.

Figure 2-1 illustrates the tunneling transmission of a TE-polarized incident wave. The wave number  $k$  is given by

$$k = nk_0 = n \frac{2\pi}{\lambda_0} \quad (2.1)$$

where  $k_0$  and  $\lambda_0$  are, respectively, wave number and wavelength in air, and  $n$  is the refractive index of the dielectric media. The wave vector  $\mathbf{k}$  makes an angle  $\theta$  with the dielectric/air interface, and has components  $k_z$  and  $k_\perp$  parallel and perpendicular to the interface, respectively, i.e.,

$$k_z = nk_0 \cos \theta \quad (2.2)$$

$$k_\perp = nk_0 \sin \theta \quad (2.3)$$

and

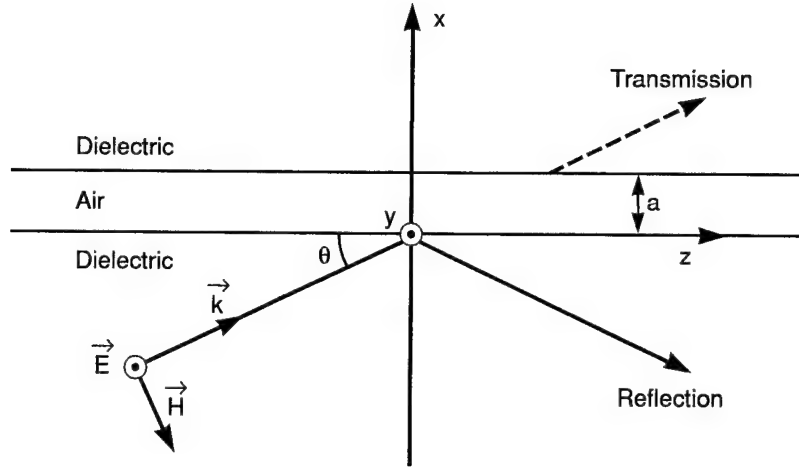


Figure 2-1. Illustration of evanescent-wave tunneling transmission. A TE wave is shown in which the electric field is perpendicular to the plane of incidence (the page). In the case of a TM wave (not shown), the  $\mathbf{H}$  field is perpendicular to the plane of incidence.

$$k_z^2 + k_{\perp}^2 = n^2 k_0^2 \quad (2.4)$$

When  $\theta$  is sufficiently small, i.e., when  $(\pi/2) - \theta$  is larger than the critical angle  $\sin^{-1}(1/n)$ ,  $k_z$  exceeds  $k_0$  and gives rise to the evanescent wave ( $\propto e^{-\beta x}$  in the absence of the second dielectric) on the air side with

$$k_z^2 - \beta^2 = k_0^2 \quad (2.5)$$

Combining Equations (2.2) and (2.5), we have

$$\beta^2 = (n^2 \cos^2 \theta - 1) k_0^2 \quad (2.6)$$

To determine the tunneling transmissivity, boundary conditions of the continuity of the tangential components of  $\mathbf{E}$  and  $\mathbf{H}$  fields are considered. In the case of a TE wave, as illustrated in Figure 2-1, the

electric field has only tangential component, i.e.,  $E = E_y$ . The tangential component of  $\mathbf{H}$  is  $H_z$  and its continuity translates into the continuity of  $\partial E_y / \partial x$  as given by the Maxwell's equation

$$\nabla \times \mathbf{E} = -\mu \partial \mathbf{H} / \partial t \quad (2.7)$$

which presently reduces to

$$\partial E_y / \partial x = i\omega \mu H_z \quad (2.7a)$$

Here,  $\omega$  is the frequency of the light wave, and  $\mu$  is the magnetic permeability, which is taken as unity for the present nonmagnetic media. The boundary conditions, i.e., the continuity of  $E$  and  $\partial E / \partial x$ , are therefore mathematically identical to those of a quantum mechanical wave function, and give rise to an analogous tunneling transmissivity [10]:

$$T_E = \left[ 1 + \frac{(k_{\perp}^2 + \beta^2)^2}{4k_{\perp}^2 \beta^2} \sinh^2 \beta a \right]^{-1} \quad (2.8)$$

The tunneling transmissivity for TM waves, however, is different. The  $\mathbf{H}$  field now has only tangential component,  $H_y = H$ . The tangential component of  $\mathbf{E}$  is  $E_z$ , and can be related to the derivative of  $H_y$  by the Maxwell's equation

$$\nabla \times \mathbf{H} = \epsilon \partial \mathbf{E} / \partial t \quad (2.9)$$

or

$$\partial H_y / \partial x = -i\omega \epsilon E_z \quad (2.9a)$$

where  $\epsilon$  is the dielectric constant of the medium and  $\epsilon = n^2$  ( $n = 3.31$  for GaP at  $\lambda_0 = 0.633 \mu\text{m}$  [11]). The continuity of  $E_z$  therefore becomes the continuity of  $\partial H / n^2 \partial x$ , which actually means a large discontinuity of  $\partial H / \partial x$  because of the change in the refraction index from dielectric to air. The boundary matching procedure then yields a tunneling transmissivity:

$$T_M = \left[ 1 + \frac{(k_{\perp}^2/n^4 + \beta^2)^2}{4k_{\perp}^2\beta^2/n^4} \sin^2 h^2 \beta a \right]^{-1} \quad (2.10)$$

Mathematically equivalent expressions were previously derived by using a transmission-line analogy [12]. As shown in Figure 2-2, equivalent transmission occurs for air gaps one order of magnitude smaller than those of the corresponding TE wave.

Experiment has been carried out to test the theory quantitatively. Samples containing artificial air gaps were prepared by using commercial one-side polished GaP(100) single-crystal wafers of 300- $\mu\text{m}$  thickness. The material was cleaved into strips of 1-mm length (z-direction) and 1-cm width (y-direction). Shallow recesses of 200- $\mu\text{m}$  width (defined lithographically) were etched by using a mixture of  $\text{K}_3\text{Fe}(\text{CN})_6$ , KOH, and  $\text{H}_2\text{O}$ . Calibrated etch rate was used, and a series of samples with recesses of 10- to 80-nm depths were etched by timing. The actual etch depths were measured by stylus profiling. Each etched piece together with a bottom piece (50% longer, unetched) were thoroughly cleaned. Liquid (methanol) surface tension was then used to pull the two pieces to very close contact [3], and the etched recess became a relatively large air gap, as illustrated in Figure 2-3.

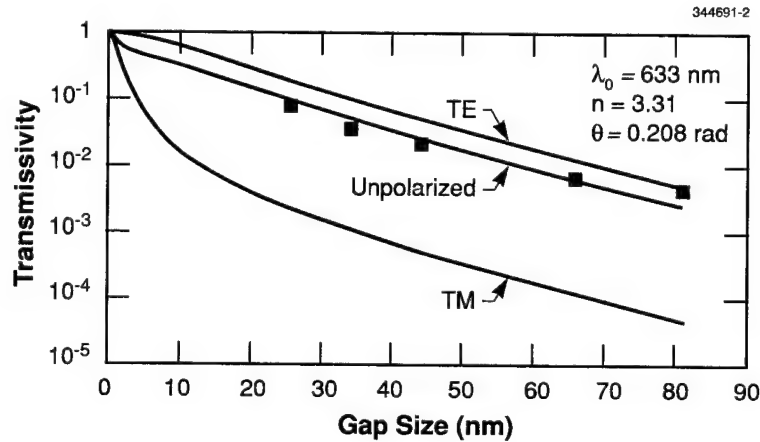


Figure 2-2. Comparison of experimental tunneling transmissivity with theory. Note that better agreement is obtained when the polarization effect is included.

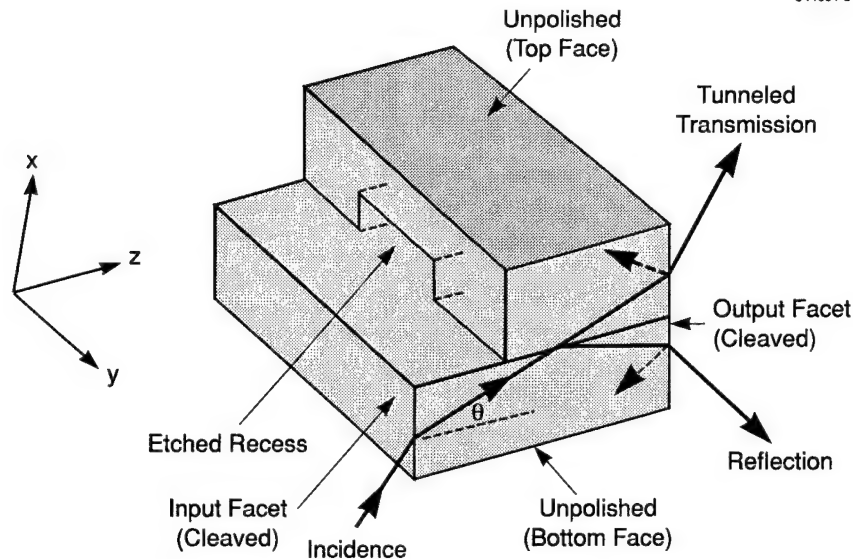


Figure 2-3. Test sample for measurement of evanescent-wave tunneling. The sample is bonded GaP/GaP, which contains an independently measured etched recess.

The bottom piece was typically 1.5 mm long in order to allow one single pass of the laser beam with an angle  $\theta$  of  $\sim 0.2$  rad, as illustrated in Figure 2-3. Note that the top and bottom faces of this test structure were intentionally left unpolished in order to scatter the back-reflected beams, shown by dashed lines in Figure 2-3. This was necessary because of the rectangular sample geometry, which can bounce the back-reflected beams and contaminate the output beams. With scattering, the back-reflected beams would be rendered a broad background and would become negligible when a small-area detector is used for the measurement of the output beams.

The experimental setup is illustrated in Figure 2-4, in which a spherical lens of 36-mm focal length was used to focus a helium-neon laser beam (originally 1-mm diameter) into the input facet of the bottom piece. The sample was mounted on one end of an aluminum rod where the rod had been cut and shaped to hold the sample without interfering with the input and output beams. This arrangement allows the sample to be rotated for any desirable incident angle. The aluminum rod was held by a micropositioner, so that the sample position can be accurately adjusted.

A silicon detector manufactured by Ophir Optonics (Jerusalem, Israel), Model No. PD200, was used to measure the powers of the output beams. The detector was specially made for the 633-nm wavelength and was capable of calibrated measurement for beam powers from 1 nW (noise level) to

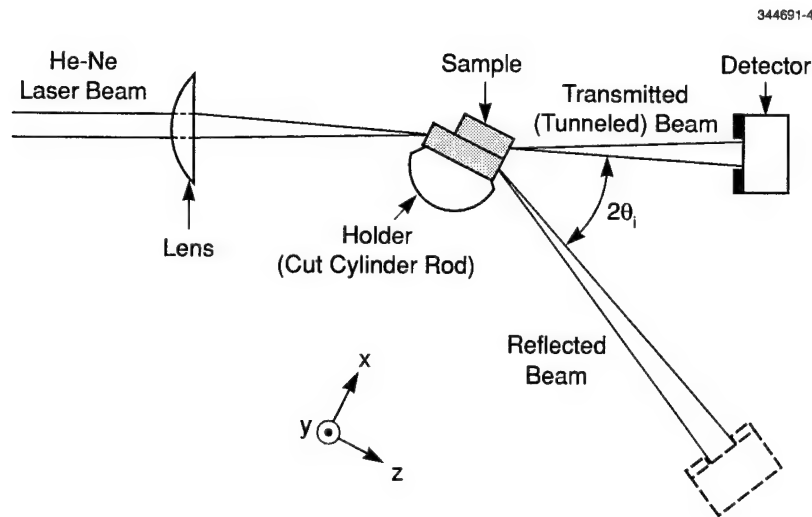


Figure 2-4. Experimental setup for measurement of evanescent-wave tunneling. The setup allows accurate sample orientation and positioning, and the tunneling measurement can be carried out in regions with and without the etched recess.

200 mW. Metal washers were mounted to block most of the 10-mm-diameter detector area to make an aperture of 2.6-mm diameter, which was sufficient for the output beams and would minimize the error caused by the background. The detector was attached to a metal fixture held by a micropositioner so that the detector could be properly aligned to fully capture either of the output beams. The powers of both the tunneled and reflected beams were measured. The sample was then moved in fine steps in the  $y$ -direction and the measurement was repeated in order to scan across the etched recess.

Figure 2-5 shows the measured powers of the tunneled and the reflected beams across a sample with an etched recess of 24 nm and a beam angle  $\theta$  of 0.208 rad. Note that outside of the etched recess the tunneled beam power is approximately 3 times that of the reflected beam, indicating a very small gap afforded by the tight molecular force bonding. In the region inside of the etched recess, the tunneled beam weakens substantially, with the missing power appearing in the strengthened reflected beam.

Table 2-1 summarizes the measurement of the bonded region (outside of the etched recess) for a series of samples measured at  $\theta = 0.208$  rad. Note that the measured transmissivity values are nearly the same (0.76) in this series of samples and correspond to a consistent theoretical air gap  $a_0$  of 1.3-nm thickness. The same  $a_0$  value was obtained in one separate experiment in which a smaller beam angle of  $\theta = 0.093$  rad was used and a transmissivity of 0.57 was measured.

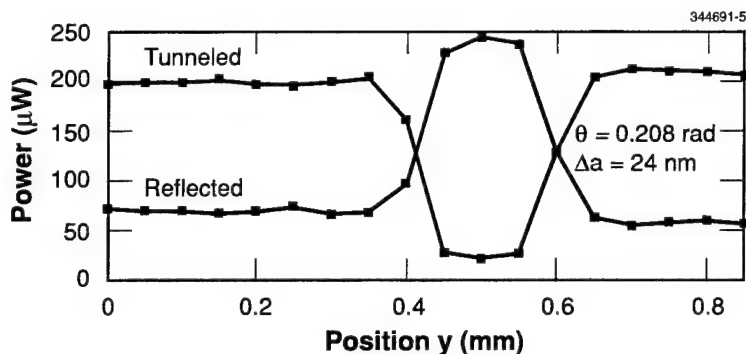


Figure 2-5. Measured intensities of tunneled and reflected beams across a sample. Note that the tunneled beam is  $\sim 3$  times that of the reflected beam in the bonded region, but reduces to 0.1 times in the recessed region, i.e., region of a larger air gap.

Table 2-2 summarizes the measurement inside the etched recesses in the same series of samples as in Table 2-1. The  $\Delta a$ 's listed in the second column are the recesses measured by stylus profiling prior to bonding. (The total gap size  $a$  is given by  $a_0 + \Delta a$ .) The beam powers and the corresponding transmissivities are listed in the next three columns. The data points in Figure 2-2 plot the measured transmissivity  $T$  vs the air gap thickness  $a$ . Note that  $T_E$  alone consistently overestimates the transmissivity, but  $(T_E + T_M)/2$  brings much better agreement with experiment.

The strong linear polarization of the tunneled beam as predicted by the theory was confirmed by inserting a polarizer foil in the output beam paths. The tunneled beam was nearly entirely extinguished when the polarizer was rotated to a proper orientation.

A comprehensive electromagnetic theoretical treatment has been presented for the evanescent light-wave tunneling across small air gaps between wafer-bonded dielectric plates. It reveals a strong polarization effect and shows that the tunneling process can be used for quantitative measurement of nanometer gaps. The theoretically predicted transmissivity and polarization showed good agreement with experiment using 20–80-nm gaps prepared by modern microlithography and wafer-bonding techniques. The theory further indicates small gaps (1.3 nm) comparable to atomic distances between bonded GaP/GaP.

Z. L. Liao  
A. A. Liao\*

---

\*Author not at Lincoln Laboratory.

**TABLE 2-1**  
**Determination of Air Gap Between Tightly Bonded GaP/GaP**

Sample	Tunneled Beam ( $\mu W$ )	Reflected Beam ( $\mu W$ )	Transmissivity $T$ (Exp.)	Air Gap $a_0$ (Theory) (nm)
2	203	66	0.75	1.28
3	202	71	0.74	1.36
4	222	60	0.79	1.12
6	219	62	0.78	1.16
7	216	75	0.74	1.34

**TABLE 2-2**  
**Test of Theory**

Sample	Etched Recess $\Delta a$ (nm)	Tunneled Beam ( $\mu W$ )	Reflected Beam ( $\mu W$ )	Transmissivity $T$ (Exp.)	Transmissivity $T$ (Theory)
2	24	28	248	0.082	0.096
3	33	10	263	0.037	0.051
4	43	6	274	0.022	0.026
6	65	2	288	0.007	0.006
7	80	1.4	300	0.005	0.003

## REFERENCES

1. See, for example, E. Yablonovitch, D. M. Hwang, T. J. Gmitter, L. T. Florez, and J. P. Harbison, *Appl. Phys. Lett.* **56**, 2419 (1990).
2. V. Lehman, K. Mitani, R. Stengl, T. Mii, and U. Gösele, *Jpn. J. Appl. Phys.* **28**, L2141 (1989).
3. Z. L. Liau, *Appl. Phys. Lett.* **77**, 651 (2000).
4. Z. L. Liau and D. E. Mull, *Appl. Phys. Lett.* **56**, 737 (1990).
5. Y. H. Lo, R. Bhat, D. M. Hwang, C. Chua, and C-H. Lin, *Appl. Phys. Lett.* **62**, 1038 (1993).
6. D. I. Babic, J. J. Dudley, K. Streubel, R. P. Mirin, J. E. Bowers, and E. L. Hu, *Appl. Phys. Lett.* **66**, 1030 (1995).
7. A. R. Hawkins, W. Wu, P. Abraham, K. Streubel, and J. E. Bowers, *Appl. Phys. Lett.* **70**, 303 (1997).
8. L. Gordon, G. L. Woods, R. C. Eckardt, R. R. Route, R. S. Feigelson, M. M. Fejer, and R. L. Byer, *Electron. Lett.* **29**, 1942 (1993).
9. F. A. Kish, F. M. Steranka, D. C. DeFever, D. A. Vanderwater, K. G. Park, C. P. Kuo, T. D. Osentowski, M. J. Peanasky, J. G. Yu, R. M. Fletcher, D. A. Steigerwald, M. G. Craford, and V. M. Robbins, *Appl. Phys. Lett.* **64**, 2839 (1994).
10. See, for example, L. I. Schiff, *Quantum Mechanics*, 3rd ed. (McGraw-Hill, New York, 1968), p. 100.
11. E. Palik, ed., *Handbook of Optical Constants of Solids* (Academic, New York, 1985), p. 459.
12. D. H. Staelin, A. W. Morgenthaler, and J. A. Kong, *Electromagnetic Waves* (Prentice Hall, Englewood Cliffs, N.J., 1994), p. 258.

### 3. SUBMICROMETER TECHNOLOGY

#### 3.1 FABRICATION OF T-GATE STRUCTURES FOR GaN FIELD-EFFECT TRANSISTORS

GaN is a wide-band-gap semiconductor that offers the potential for an order-of-magnitude improvement in the power density of power amplifiers in X-band transmit/receive (T/R) modules. To achieve the optimum performance from a field-effect transistor (FET) fabricated on GaN, a T-gate structure, which has a narrow foot and a wide top, is desired. The narrow foot of the T-gate provides a short gate length, thus allowing a high cutoff frequency. The wide top of the gate provides low resistance, thus allowing high gain.

It is desirable to pattern the T-gate as a single lithographic step to minimize the number of processing steps and to assure the alignment of the top and bottom of the T. Traditionally, T-gate structures are fabricated using electron-beam lithography with multiple layers of polymethyl methacrylate (PMMA) and copolymers of methyl methacrylate (CoMMA) serving as the resist [1]. The greater sensitivity of the CoMMA vs PMMA causes the layer of CoMMA resist above PMMA resist to develop to a larger dimension. This provides a means for producing the desired T shape. To produce the desired undercut profile necessary for good metal lift-off, a third resist layer (typically PMMA) is applied above the CoMMA. It is possible to simultaneously optimize the exposure and the resist layers to produce the desired developed dimensions in all three resist layers. Doing so, however, requires significant experimentation [2]. Difficulties arise because the sensitivities of PMMA and CoMMA are similar—typically only a factor of 2–3 different. Changing the exposure to produce a change in one resist's dimension, will invariably have an effect on the other's dimensions.

The approach we have used follows work done by Chen et al. [3] and involves a chemically amplified resist, UV5, applied above an e-beam resist, ZEP. In this arrangement the UV5 defines the top of the gate while the ZEP defines the foot. Because the UV5 resist is much more sensitive (by a factor of 6) than the ZEP resist, the exposure of the UV5 can be varied without significantly affecting the ZEP resist. In addition, the two resists are developed independently, the UV5 in an aqueous base solution and the ZEP in an organic solvent. This allows the separate optimization of the processes for the two resist layers, greatly simplifying the experimentation needed for the production of the desired profile. The ability to separately optimize the two resist processes also allows processes to be chosen that have a large degree of robustness. Furthermore, variations in the top of the gate, such as producing asymmetrical or  $\Gamma$ -gates can easily be made without having to worry about causing a change in the dimension of the foot of the gate.

Figure 3-1 shows the final process used to pattern the T-gates. The ZEP layer is spun to a thickness of  $0.35\text{ }\mu\text{m}$  and the UV5 to a thickness of  $1.0\text{ }\mu\text{m}$ . During patterning, a nominal  $0.1\text{-}\mu\text{m}$ -wide feature is exposed with a heavy dose of  $390\text{ }\mu\text{C}/\text{cm}^2$  at the center of the gate. This will result in a  $0.2\text{-}\mu\text{m}$ -wide gate foot in the developed ZEP. An additional  $1.0\text{-}\mu\text{m}$ -wide feature is exposed at a dose of  $30\text{ }\mu\text{C}/\text{cm}^2$  to define the  $1.0\text{-}\mu\text{m}$ -wide gate top in the UV5. A relatively long development of 3 min in standard develop

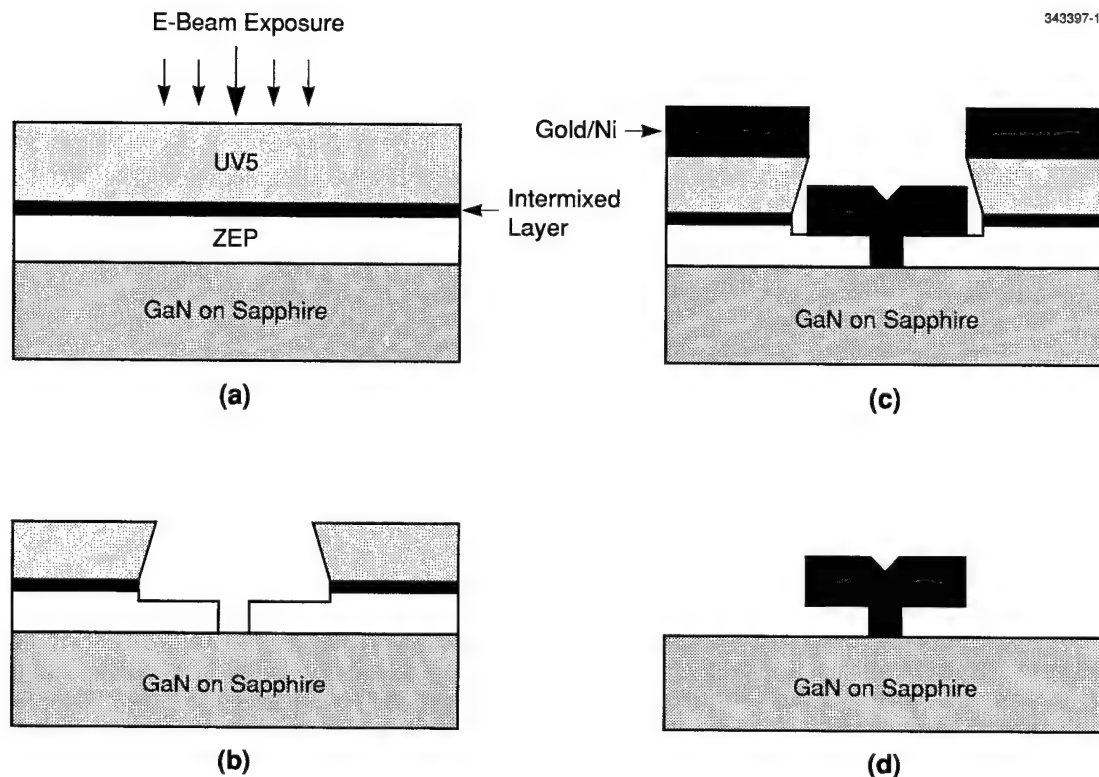


Figure 3-1. Process flow for fabrication of T-gate: (a) application of resist layers and e-beam exposure, (b) development and plasma etch steps, (c) metal deposition, and (d) T-gate remaining after lift-off.

(LDD26W) is used for the development of the UV5. The UV5 dose and development procedure was chosen to produce the desired reentrant profile in the UV5 resist. After development of the UV5 (and a plasma ash that will be discussed), the ZEP layer is developed in xylenes for 30 s. The choice of xylenes as the developer for ZEP is critical because xylenes, unlike most organic developers, do not dissolve the UV5. An additional quick plasma ash is used after ZEP development to remove any resist scum that may be left. After development and both plasma ashing steps,  $\sim 2500 \text{ \AA}$  of ZEP remain. This thickness of ZEP defines the height of the gate foot.

After the development of the resists, layers of  $500 \text{ \AA}$  of Ni and  $4500 \text{ \AA}$  of Au are deposited by evaporation. The Ni provides the necessary Schottky contact while the Au provides low transverse resistance. Lift-off is done with acetone followed by chlorobenzene to remove the UV5 and ZEP layers, respectively.

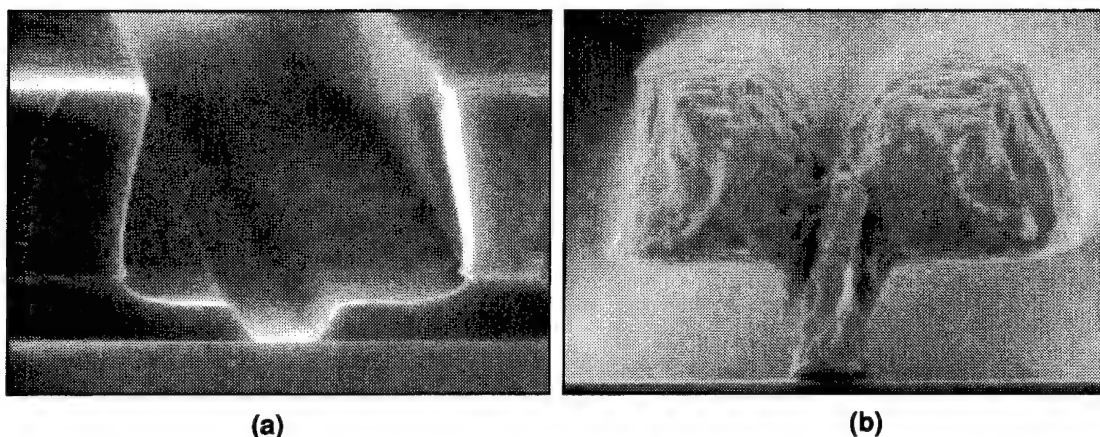


Figure 3-2. Electron micrographs of (a) resist profile and (b) completed T-gate.

One difficulty with this method is caused by the intermixing of the UV5 and ZEP. The spin casting of the UV5 directly on the ZEP produces a thin intermixed layer that is insoluble in either the UV5 developer or the ZEP developer. One solution for this problem [3] is to use a thin (200 Å) layer of evaporated Al to separate the UV5 and ZEP. We, however, have found that the Al layer can cause its own difficulties because the developer used for the UV5 also dissolves the Al. At times the Al will dissolve in such a manner that the Al and the UV5 separate from the ZEP. To avoid this failure mode, we spin the UV5 directly on the ZEP. Between the development of the UV5 and the ZEP resists, a quick plasma ash is used to remove the intermixed layer. Once this intermixed layer is removed the ZEP can be developed normally.

Figure 3-2(a) shows the profile of the resist layers after development. The desired 0.2- $\mu\text{m}$ -wide feature has been produced in the ZEP as well as the 1.0- $\mu\text{m}$ -wide feature in the UV5. Note that the UV5 has the desired reentrant profile, which improves the ability to do lift-off. Figure 3-2(b) shows the final T-gate after metallization and lift-off. The final widths of the gate foot and top are 0.21 and 1.08  $\mu\text{m}$ , respectively. The gate shown here was fabricated on Si, but similar devices have been fabricated on GaN. The fabrication of the T-gate on GaN is performed identically to the fabrication on Si, with no need for changing the processing or exposure doses. In addition,  $\Gamma$ -gates were fabricated with no changes other than the placement of the gate top defining exposure. This gives an indication that our fabrication method offers a certain degree of flexibility and robustness.

As the process for the T-gate fabrication was being developed, the device layout and design were done in parallel. The first FETs on GaN substrates using this process are currently being fabricated.

S. J. Spector	L. J. Mahoney
K. M. Molvar	D. M. Lennon

### 3.2 CONTROLLED CONTAMINATION OF OPTICS UNDER 157-nm LASER IRRADIATION

The drive of the semiconductor industry towards smaller device dimensions has challenged lithographers to print smaller patterns in photoresist. The reduction in feature size has been accomplished by utilizing progressively shorter wavelength light sources, such as 248-nm excimer lasers and, recently, 193-nm excimer lasers. During the past year, microlithography using 157-nm pulsed fluorine lasers has emerged as the leading candidate technology for circuit dimensions on the order of  $0.1\ \mu\text{m}$ . Contamination of optics with outgassing products either from resist exposure or from outgassing various materials used for construction of the projection optics is expected to be a major concern at this wavelength. Because of the higher 157-nm photon energy as compared to that at 193 nm, the dissociation cross sections of organics may be orders of magnitude higher than that at 193 nm.

For this study we have identified a number of organic molecules that had been previously found to evolve from photoresists under 193-nm irradiation [4] and introduced small amounts of these contaminants into a nitrogen gas stream that flowed over optical surfaces. We then characterized changes in transmission that occurred in the presence of contamination and 157-nm irradiation.

Figure 3-3 shows the schematic of the controlled contamination system. The system consists of the manifold for delivering contaminants into the vapor stream, shown in Figure 3-3 (top), and the laser exposure apparatus, shown in Figure 3-3 (bottom). Contaminants are delivered from saturated vapor over a liquid source. The vapor diffuses through a membrane whose permeation rate is characterized for a given cell length at a given temperature [5]. This method allows us to change contaminant sources quickly and inexpensively, without the use of high-pressure gas cylinders for gas delivery. More than 100 different permeation sources are commercially available, and new ones can be synthesized readily, provided that the source compound is a liquid with a sufficiently high vapor pressure. The amount of contaminant delivered into gas phase can be changed by operating at different cell temperatures and different dilution ratios with the carrier gas. Our gas delivery manifold utilizes three separate mass flow controllers, allowing independent control of the contaminant levels and resident times of the vapor cell, containing optics to be contaminated.

The vapor cell containing optics under study, seen in Figure 3-3 (bottom) and Figure 3-4, is irradiated with a high-repetition-rate (600 Hz) 157-nm laser, and the in-situ transmission of the cell is continuously monitored. Along with the cell, a witness  $\text{CaF}_2$  sample is irradiated to assure that any potential transmission changes are caused by adsorbed contamination and not by degradation of the sample itself. Prior to introduction of contaminants into the vapor stream, we have ascertained that no transmission degradation takes place when pure nitrogen is allowed to flow through the contaminant oven over the cell windows. These background verifications were performed for total exposure doses exceeding the maximum dose used in any contamination experiments. We also verified that the background oxygen and moisture levels in our gas manifold were below the detection limit of our analyzers ( $<200$ -ppb oxygen and  $<100$ -ppb moisture).

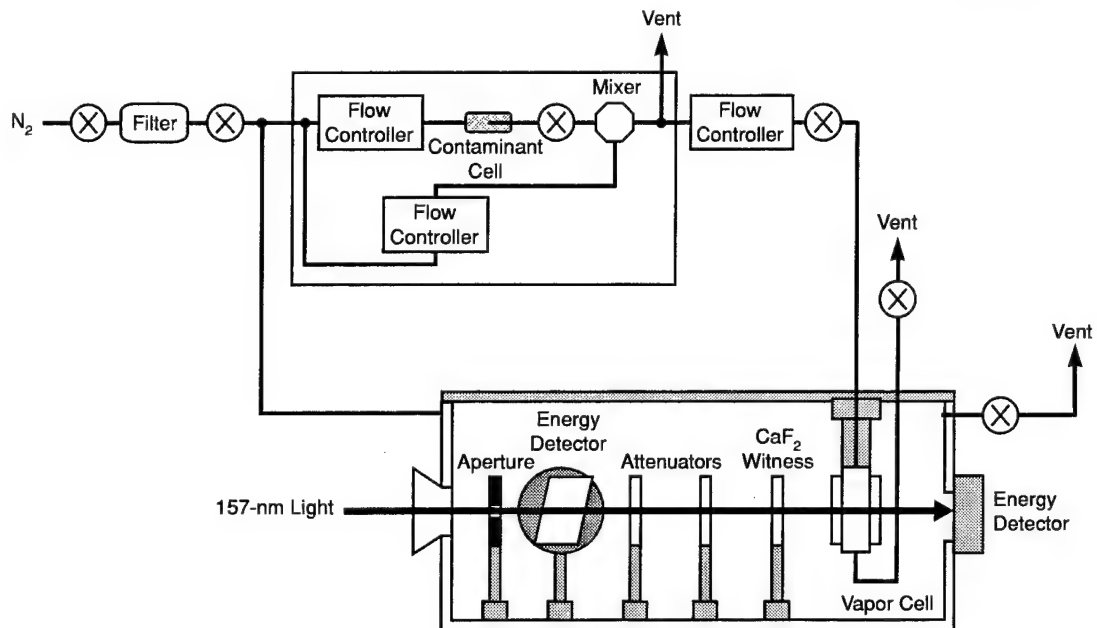


Figure 3-3. Overall view of controlled contamination system, including gas delivery manifold and laser irradiation system.

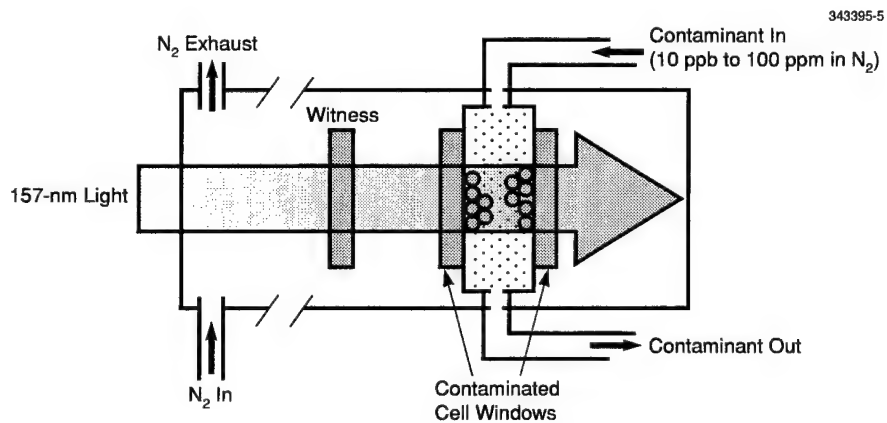


Figure 3-4. Detailed view of controlled contamination cell containing optics under study.

Figure 3-5 shows a typical contamination experiment using toluene as a gas phase contaminant at a concentration of 5 ppm. In-situ transmission measurement of the cell includes both windows; however, in the data presented here "single-window transmission" is obtained by taking the square root of the total cell transmission. The incident laser fluence for this study was  $0.5 \text{ mJ/cm}^2/\text{pulse}$  and the pulse repetition rate was 600 Hz. For the first 2 h of the experiment the contaminant was allowed to flow over cell windows, but the laser was not irradiating the cell except for a brief period of time to acquire in-situ transmission data. During those initial 2 h, no transmission degradation of the cell windows was observed. The slightly lower initial transmission of the cell windows as compared to the witness sample may be caused by gas phase absorption of toluene vapor over the 1-cm cell length.

After 2 h, the laser was allowed to irradiate the cell continuously. We observed a pronounced transmission drop of cell windows with increased laser dose, whereas transmission of the witness sample remained unchanged, as shown in Figure 3-5. From the follow-up spectroscopic analysis of the contamination layer, 157-nm laser light appears to transform adsorbed toluene molecules into a graphitic overlayer which accumulates on the surface with increased dose. We verified that the contaminating layer that had been formed with the laser did not reevaporate for up to 48 h after interruption of irradiation.

After a dose of  $800 \text{ J/cm}^2$  had been delivered (corresponding to an elapsed time of 2.8 h in Figure 3-5), the flow of contaminant was turned off, and instead, pure nitrogen was allowed to flow over the cell windows as the laser continued to irradiate it. We observed gradual recovery of transmission under laser irradiation. The recovery may be due to direct laser photodesorption of surface species. It may also be caused by a photoinduced reaction of graphitic overlayer with a small amount of gas phase oxygen. We have previously reported that laser-induced cleaning of organic deposits on optics can be achieved efficiently by irradiation in the presence of gas phase oxygen [6].

Experiments similar to the one described in Figure 3-5 were performed over a wide range of laser fluences, confirming that the contamination rate scales with total dose and not with laser fluence per pulse. At contaminant levels above 1 ppm, the contamination rates appeared to scale linearly with vapor phase concentration of contaminants. At contaminant levels below 1 ppm, the forward contamination rate decreases until backward cleaning reaction, shown in Figure 3-5, becomes significant. Thus, the smallest amount of gas phase contaminant that would cause a transmission drop may be a sensitive function of residual oxygen present in the cell.

Similar contamination experiments were performed for acetone as the vapor phase contaminant. Once again, for vapor phase contamination levels above 1 ppm, transmission degradation was observed comparable to that shown in Figure 3-5.

While the contamination data obtained above are preliminary and more experiments are being performed to verify impact of various contaminants on surfaces coated with thin film coatings, it is instrumental to evaluate the potential impact of optics contamination on an optical system with a large number of optical surfaces. From our contamination experiments at the lowest observable gas phase concentration for either acetone or toluene, we extrapolated an upper limit for contamination rates at a gas

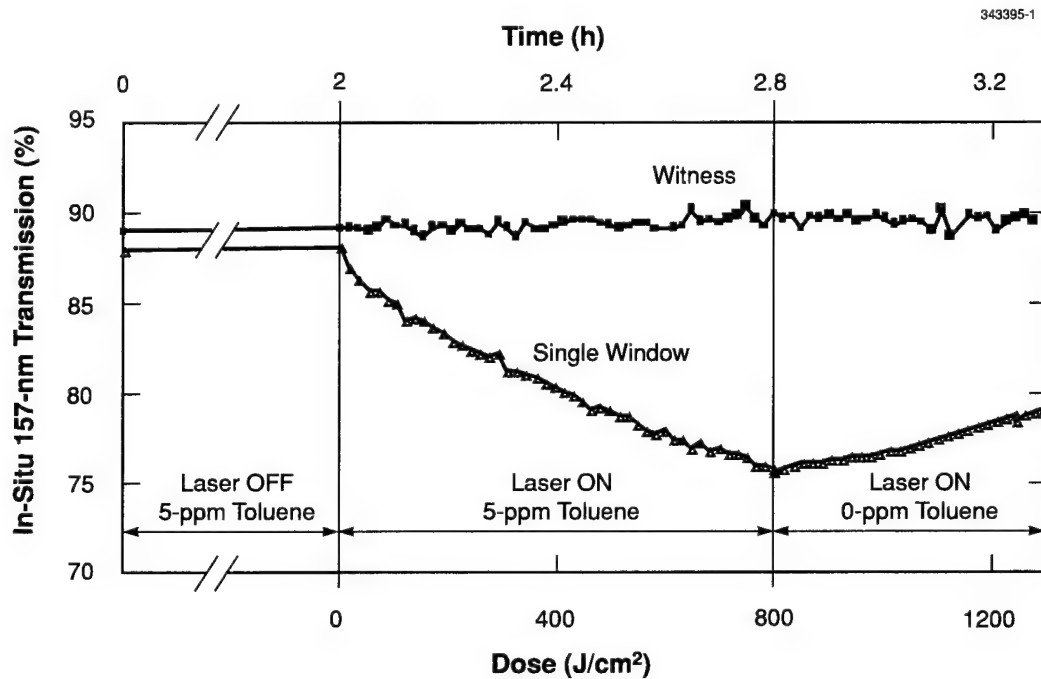


Figure 3-5. Typical controlled contamination experiment for 5 ppm of toluene, showing (a) absence of contamination without laser light but with contaminant flowing over the optics, (b) transmission degradation of optics once the laser light is turned on, and (c) cleanup of the contaminated optics with laser light once the flow of contaminant is disabled.

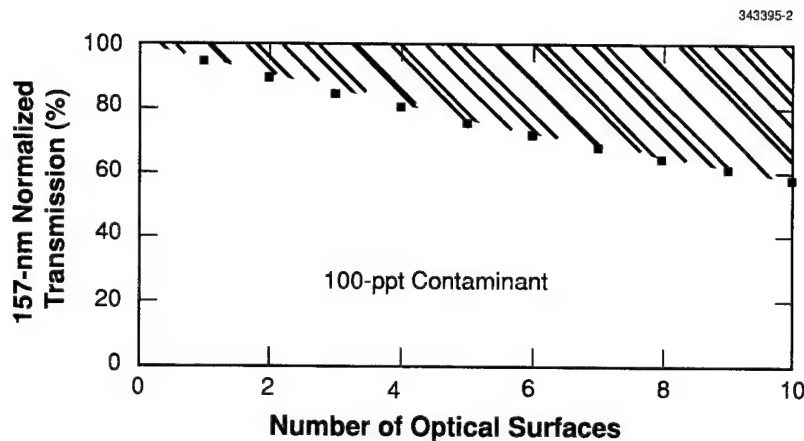


Figure 3-6. Prediction of impact of contamination on an optical system for increasing number of optical surfaces. For a given number of optical surfaces, the expected normalized 157-nm transmission is shown by a hatched range, the uncertainty arising from an extrapolation of experimental data over several orders of magnitude of gas phase contaminant concentration. The gas phase contaminant concentration is 100 ppt. The total laser dose corresponds to one month of operation in a production environment:  $10^9$  pulses at  $0.1 \text{ mJ/cm}^2/\text{pulse}$ .

phase concentration of 100 ppt. This low level of gas phase contaminant is not unrealistic for a future 157-nm projection system; however, achieving it would require careful purge design and consideration of all potential sources of outgassing that can take place in a lithographic system.

Figure 3-6 shows normalized 157-nm transmission as a function of the number of optical surfaces for an incident exposure dose equivalent to one month of system operation:  $10^9$  pulses at an incident fluence of  $0.1 \text{ mJ/cm}^2/\text{pulse}$ . The results show that even for these low contaminant levels, mitigation methods may need to be considered for systems comprising a large number of optical surfaces. In practice, a 157-nm optics purge design will be able to tolerate from 1 to 30 ppm of background oxygen concentration, depending on the pathlength of the purged enclosures. At these increased oxygen levels, the backward cleaning rate is expected to compete efficiently with the forward contamination. Nevertheless, understanding the impact of various potential gas phase contaminants on transmission degradation and quantifying competing reaction rates for cleaning and contamination remain topics of great interest to the 157-nm lithographic community.

V. Liberman  
T. M. Bloomstein  
M. Rothschild

## REFERENCES

1. P. C. Chao, P. M. Smith, S. Wanuga, J. C. M. Hwang, W. H. Perkins, R. Tiberio, and E. D. Wolf, *International Electron Devices Meeting Technical Digest* (IEEE, New York, 1983), p. 613.
2. D. R. Brambley and R. H. Bennett, *GEC J. Res.* **13**, 42 (1996).
3. Y. Chen, D. Macintyre, and S. Thoms, *J. Vac. Sci. Technol. B* **17**, 2507 (1999).
4. R. R. Kunz, V. Liberman, and D. K. Downs, *Microlithogr. World* **9** (Winter), 2 (2000).
5. VICI Metronics, Inc., Santa Clara, Calif.
6. T. M. Bloomstein, M. Rothschild, V. Liberman, and D. E. Hardy, *Proc. SPIE* **4000**, 1537 (2000).

## 4. BIOSENSOR AND MOLECULAR TECHNOLOGIES

### 4.1 EFFECTS OF FLOW-CELL GEOMETRY AND LATERAL-VELOCITY FIELDS ON ANTIGEN DELIVERY IN MICROFLUIDIC CHANNELS

Flow in microfluidic channels is usually in the laminar regime, owing to the inherently low Reynolds numbers of microfluidic geometries. The trajectories of antigen delivered into microfluidic devices are therefore predominantly axial (along the direction of flow). If molecules are small enough, diffusive transport can rapidly give rise to equilibrium distributions of reagents in small channels. However, the smaller diffusion constants of larger particles lead to limited antigen transport to channel side walls, where active sensing elements are often located; this can result in low sensitivity for devices such as microfluidic sensors. We present numerical simulation studies demonstrating the enhancement of sensitivity for microfluidic devices using two schemes: simple modifications of the flow-cell geometry, and the introduction of lateral-velocity fields.

Computational fluid dynamics simulations based on the Navier-Stokes equations were performed, using a continuum approach to allow incorporation of surface-binding effects. The continuum approach was previously validated as providing nearly identical results with the computationally more intensive Lagrangian methods for this class of problems. Flow was modeled as laminar, incompressible, and Newtonian. Variable time stepping was used to eliminate computational inefficiency, and transient mass transport and surface reactions were solved for at each time step. Second-order kinetics were used for the association reaction and first-order kinetics for the dissociation process.

Simple modifications of the flow-cell geometry can significantly enhance particle interaction with the channel side walls. As one example, surface coverage contours for a microfluidic channel with a centered-post obstacle are shown in Figures 4-1(a) and 4-1(b). They show a short-term pulse of particle binding on the post surface, where the bulk of the antigen-laden flow is incident. As time passes, the antigen settles down, with maximal binding concentrations in the area in front of the post itself. These obstacles promote binding because the formation of near-wall fluid-boundary layers slows down the particles and increases the residence time near active surfaces. This allows the diffusion mechanism additional time to direct particles from the free stream toward the active sensor sites. Interception of the flow near the center of the chamber appears to be a general method for enhancing device sensitivity. A summary of the time evolution of the averaged surface binding for all geometries considered in this study is shown in Figure 4-2. Post and cupped-post (denoted cup) structures provide the greatest sensitivity enhancement, up to 2–3 orders of magnitude over the simple “flush” geometry. Calculations have shown that inertial penetration (streamline crossing) by particles is negligible for particles of bacterial size, since the response-time scale for the particle is much smaller than that of the fluid itself. This provides additional validation for the continuum-modeling approach used in this study, since it fully accounts for the dominant boundary layer effects caused by the presence of obstacles.

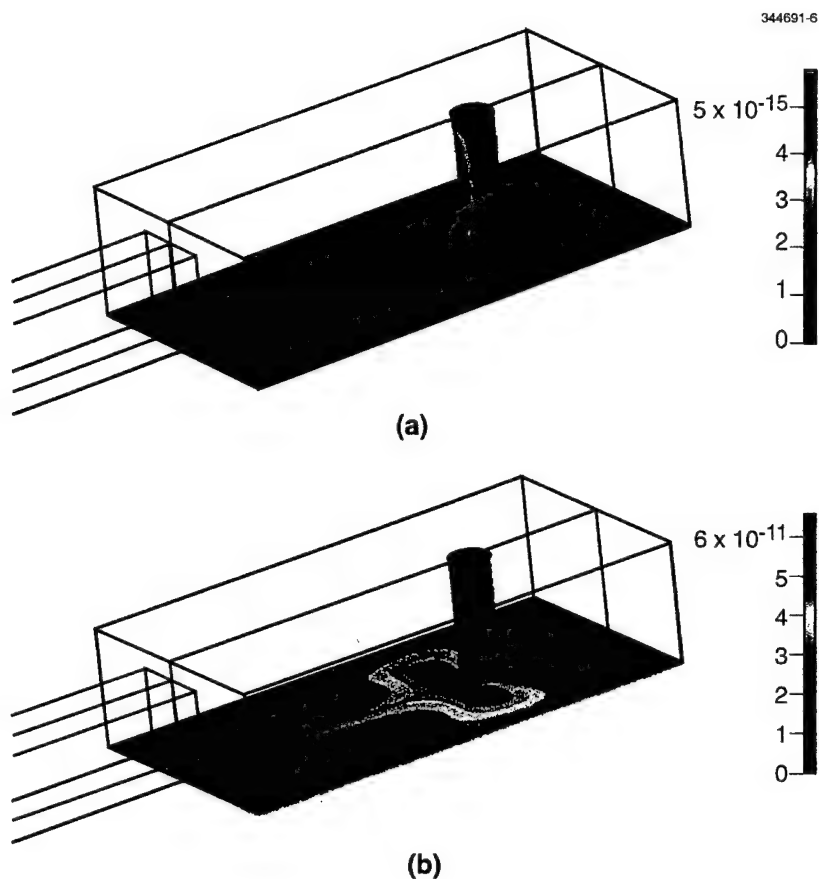


Figure 4-1. (a) An initial pulse of antigen reaches the post at early times. (b) At later times, antigen settles out in a concentrated zone in front of the post. Flow is from left to right. Note difference in color scales.

For the sample concentrations and flow rates considered, diffusion leads to only limited interaction between the incoming sample and the channel side walls. Methods of imparting lateral force to direct the particles across fluid streamlines can significantly enhance interaction with the side walls. Such lateral force can be generated by a variety of methods such as gravity, magnetic fields, electrophoresis, and

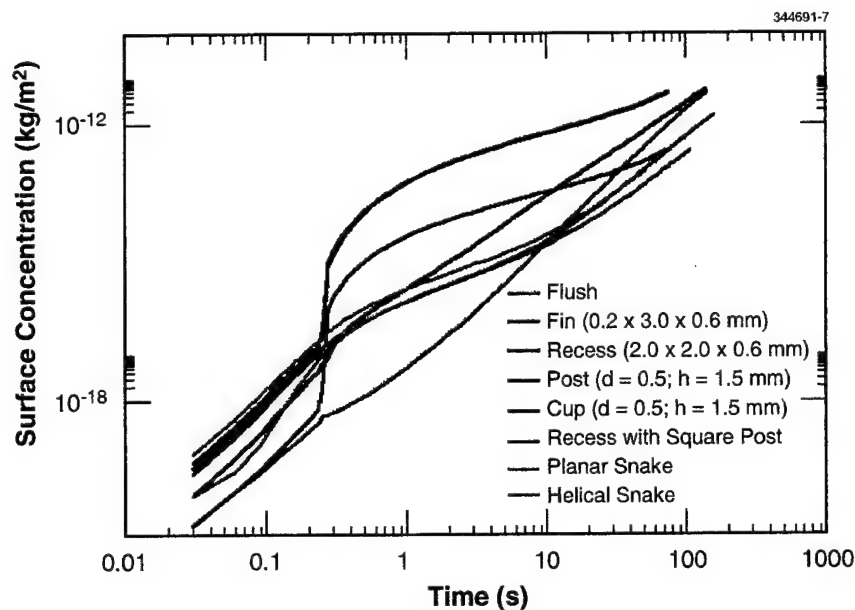


Figure 4-2. Surface binding for various flow-chamber geometries.

thermophoresis. The effects of any of these forces can be analyzed by treating them as lateral-velocity fields. The results of studies looking at the effect of lateral velocity as a generic parameter are shown in Figure 4-3, demonstrating that surface concentrations are significantly enhanced by the lateral-velocity fields. The time scales over which the greatest effects occur depend on the actual velocity; for the lateral velocities studied here, effects of 2–3 orders of magnitude are seen over the time scale 10–100 s.

In conclusion, simple modifications of the flow-cell geometry and the introduction of lateral-velocity fields both can enhance the interaction of incoming particles with channel side walls by orders of magnitude. Such effects can be important in the design of devices with microfluidic components.

A. M. Young	S. Sundaram*
V. Makhijani*	A. E. Rundell
M. A. Hollis	

---

\*Author not at Lincoln Laboratory.

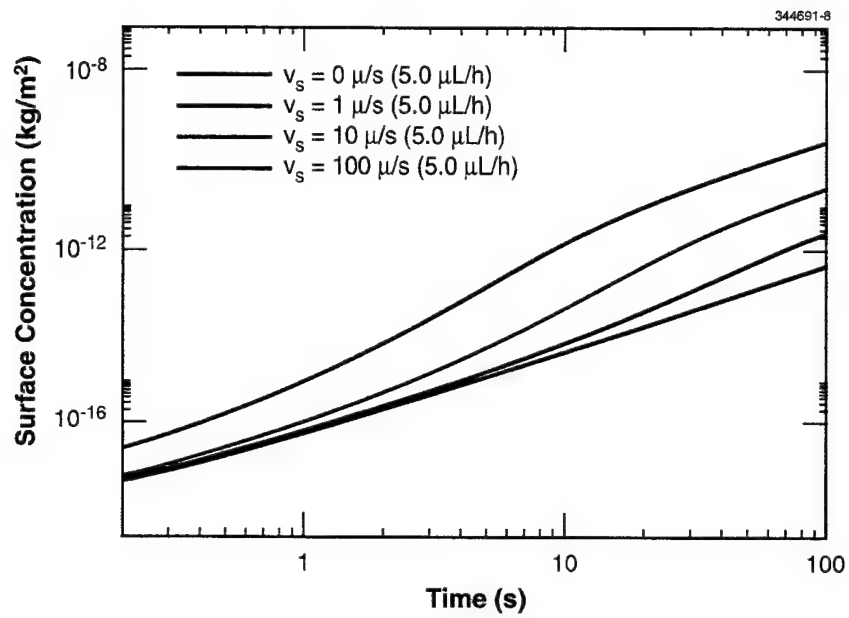


Figure 4-3. Effects of lateral velocity on surface concentration.

## 5. ADVANCED IMAGING TECHNOLOGY

### 5.1 DEVELOPMENT OF LOW-DARK-CURRENT BACK-ILLUMINATED PHOTODIODES

A program is under way to develop sensitive, low-power, and lightweight image sensors for a DARPA-sponsored micro-unmanned air vehicles (UAV) project where the sensor must image under both day- and night-illumination conditions. The approach involves development at Lincoln Laboratory of sensitive back-illuminated (BI) photodiodes, which will then be indium-bump bonded to low-noise readout electronics being developed at Rockwell Science Center. By fabricating the devices separately in this hybrid approach, the photodiode array and readout circuits can be separately optimized for low dark current and better low-light-level performance. For the proposed detector, the improvement in sensitivity compared to commercially available CMOS sensors is expected to be approximately 2 orders of magnitude.

Here, we report initial results on the development of BI low-dark-current  $p^+$ -on- $n$  photodiodes fabricated on high-resistivity ( $>3000 \Omega \text{ cm}$ ,  $n$ -type) Si substrates. The selected diode geometry for this program is illustrated in Figure 5-1(a). An  $\sim 8\text{-}\mu\text{m}$ -diameter heavily doped  $p$ -type region ( $16\text{-}\mu\text{m}$  pixel) is formed by boron ion implantation through a  $\text{SiO}_2$  field oxide opening in a self-aligned fashion. A heavily doped channel-stop region ( $n$ -type phosphorus implant) surrounds the diode junction area at a separation distance  $S$ . Ultimately, the Si substrate wafer will be thinned to a thickness of  $40\text{--}100 \mu\text{m}$  in order to enable a fully depleted diode array at low applied reverse bias ( $<10 \text{ V}$ ). A thin  $n^+$  substrate region is formed on the wafer BI side by ion implantation and furnace anneal.

In general, there are three major contributions to the overall dark current of a diode such as that described above: (1) thermal generation in the bulk depletion layer, (2) thermal generation at the depleted Si-SiO<sub>2</sub> interface, and (3) the combined action of thermal generation at the back-side contact of the wafer and bulk diffusion from neutral regions outside the depletion layer. Detailed analyses of each of these components is described elsewhere [1]–[3]. In general, bulk generation current from the depletion layer will exhibit a bias dependence while surface and diffusion generation currents do not.

Bulk generation currents can be minimized by back-side gettering to maintain lifetime for high-temperature-processed wafers and by thermal processing techniques designed to minimize both slip and stress-induced bulk defects. In addition, tapered  $p$ -type doping profiles can be used to lower the electric field in the high-field region between the junction and channel-stop regions. Surface generation contributions to the dark current that originate from traps at the Si-SiO<sub>2</sub> interface can be lowered by avoiding plasma processing, which can induce higher densities of interface states, and by using an  $\text{H}_2$  anneal after contact metallization, which is a well-known technique used to passivate interface states. From the diode geometry standpoint, surface generation currents depend on the diode perimeter. They can be minimized by making both the diode junction and the junction/channel-stop separation ( $S$  in Figure 5-1) as small as possible within the design constraints imposed by other desired diode parameters such as breakdown, capacitance, and metallization footprint.

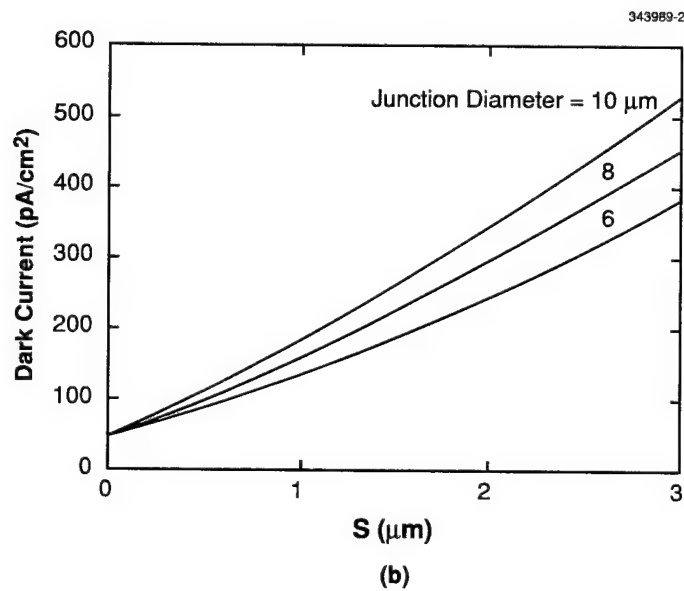
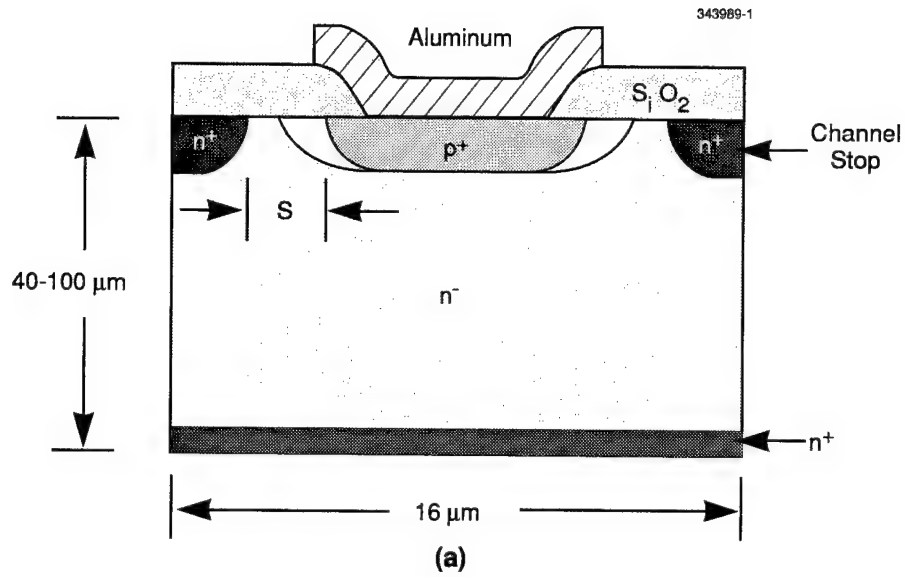


Figure 5-1. (a) Cross section of proposed photodiode geometry.  $S$  is the lateral  $p^+n$  junction channel-stop separation distance. (b) Calculation of dark current as a function of  $S$  ( $\mu\text{m}$ ) based on an empirical model for the surface and bulk generation contributions to the diode leakage current for three different junction diameters.

For large diode arrays fabricated on high-quality long-lifetime material, surface generation is expected to dominate over bulk generation contributions to the dark current. Charge-coupled devices (CCDs) exhibiting bulk generation leakage currents less than  $\sim 50 \text{ pA/cm}^2$  have been fabricated using the process considerations outlined above [4]. Surface generation leakage currents on the order of  $1 \text{ nA/cm}^2$  per micron of  $S$  have been observed on these same wafers. With this empirical model, one can calculate the expected overall (bulk plus surface) dark current dependence on  $S$  for various diode junction diameter choices allowed by the  $16\text{-}\mu\text{m}$ -pixel design. This is shown in Figure 5-1(b). For each curve, the junction diameter is fixed while  $S$  is varied by changing the channel-stop geometry by the appropriate amount. To achieve an overall dark current of  $<150 \text{ pA/cm}^2$ , one needs to keep  $S < 1 \mu\text{m}$  for a  $16\text{-}\mu\text{m}$ -pixel diode.

Figures 5-2 and 5-3 show the results of dark current measurements made on test photodiodes. For the measurements illustrated in Figure 5-2, the dark current for a single interior diode from an array of identical diodes was measured as a function of reverse bias from 0 to 10 V (bias applied through the substrate). The neighboring diodes were connected together and separate dark current curves were obtained with these "guard" diodes biased from  $-2$  to  $+2 \text{ V}$  (1-V increments) with respect to the current-monitoring diode. With this method, in addition to observing the bias dependence, one can qualitatively determine if the dominant contribution to the dark current is bulk or surface related. The surface contribution should be nearly independent of the guard diode bias, and thus if the currents for each of the curves are within a small fraction of each other, one could conclude that the surface contribution dominates. On the other hand a wide "spread" of values could indicate large contributions from the bulk and/or back surface.

Figure 5-3 compares the dark currents of four wafers taken with both guard and interior diodes at 0 V (substrate bias 0–10 V as in Figure 5-2). Three of the wafers are BI diodes with the substrates thinned to 50 and  $100 \mu\text{m}$  as indicated in the figure. The fourth curve is that obtained on a full-thickness ( $650 \mu\text{m}$  and front-illuminated process) diode wafer. The  $50\text{-}\mu\text{m}$  BI diode exhibits a dark current  $\sim 300\text{--}400 \text{ pA/cm}^2$ . The measured current (tens of femtoamps) is just above the measurement limit of the instrument, which accounts for the noise in the data. The  $100\text{-}\mu\text{m}$  BI diodes exhibit a slight bias dependence with currents becoming smaller with increasing reverse bias. This is likely owing to the lowering of diffusion currents generated outside and below the depletion edge of the guard diode region, which are effectively "pinched off" as the depletion region expands with bias. At 10 V, the wafer is fully depleted. A second  $100\text{-}\mu\text{m}$  BI diode exhibits a dark current in the range  $200\text{--}300 \text{ pA/cm}^2$ . The full-thickness wafer shows a dark current of  $\sim 700 \text{ pA/cm}^2$  with much of this excess current probably arising from diffusing carriers originating outside the guard diode region and below the measured photodiode. We estimate that the actual dark current for this wafer (in a large array) would be at least 50% lower or  $\sim 350 \text{ pA/cm}^2$ . For large fully depleted BI diode arrays, diffusion currents such as those observed for the full-thickness wafer should contribute minimally to the overall dark current. By aggressively minimizing the junction/channel-stop separation ( $S$  above) to  $<1 \mu\text{m}$ , we believe dark current levels at the program requirements of  $100\text{--}200 \text{ pA/cm}^2$  can be achieved with our current process.

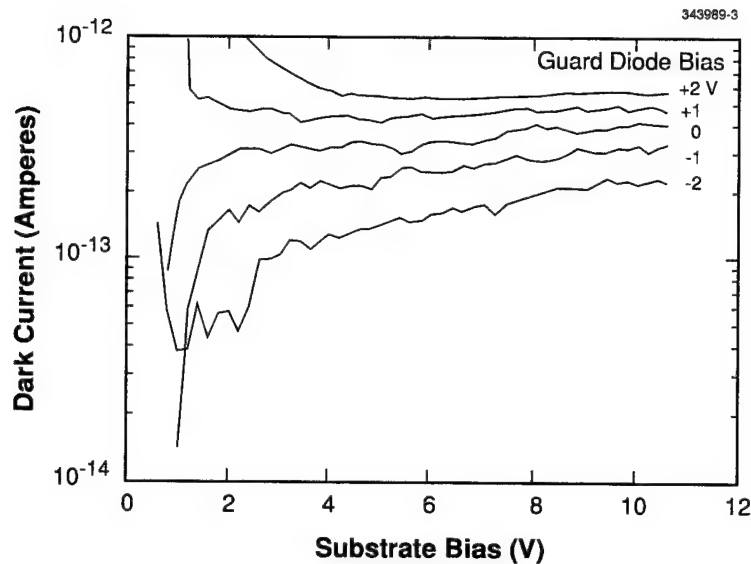


Figure 5-2. Measured dark current of single interior diode as a function of reverse (applied to the substrate) bias. The measured diode is surrounded by an array of diodes that are biased at the voltage (with respect to the measured diode) indicated in the figure.

Our current experience with CCDs shows that dark currents for laser-annealed BI devices are substantially higher than that observed for front-illuminated devices. A very important result here is that our BI diodes have dark currents at least comparable to those obtained using the front-illuminated process. This accomplishment is primarily the direct result of using a shallow phosphorus implant and furnace oxidation-anneal for the BI-side  $n^+$  region.

D. D. Rathman  
A. H. Loomis

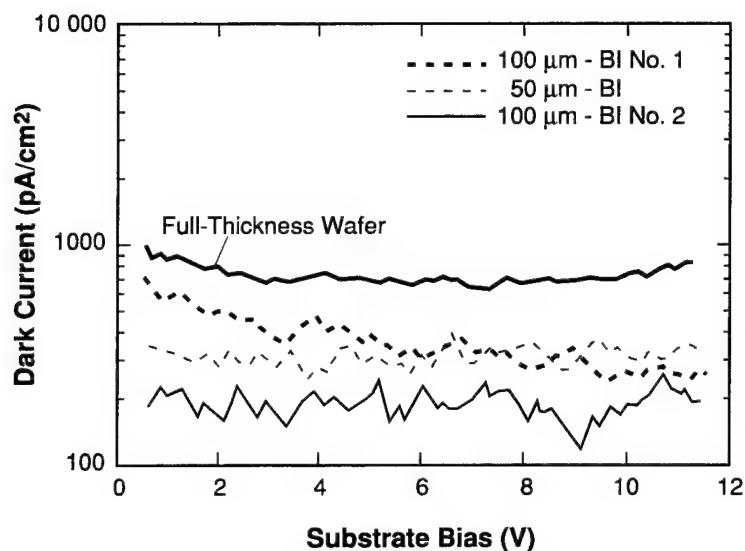


Figure 5-3. Measured dark current of identical geometry diodes for four different wafers, three back-illuminated wafers (50–100  $\mu\text{m}$  thick) and one full-thickness wafer. Surrounding “guard” diodes were biased at the same voltage as the measured diode.

#### REFERENCES

1. G. Vanstraelen, K. De Baccker, I. Debusschere, C. Claeys, and G. Declerk, *Nucl. Instrum. Meth. Phys. Rev. A* **288**, 48 (1990).
2. A. S. Grove and D. J. Fitzgerald, *Solid-State Electron.* **9**, 783 (1966).
3. G. Verzellesi, G. F. Dalla Betta, L. Bosisio, M. Boscardin, G. U. Pignatelli, and G. Soncini, *IEEE Trans. Electron Devices* **46**, 817 (1999).
4. B. E. Burke and S. A. Gajar, *IEEE Trans. Electron Devices* **38**, 285 (1991).

## 6. ANALOG DEVICE TECHNOLOGY

### 6.1 DEMONSTRATION OF ACCURATE COMPENSATED NORMAL-METAL CHIRP FILTERS ON ALUMINA SUBSTRATES

Compressive receivers achieve the high sensitivity typical of a narrowband receiver while covering a wide instantaneous bandwidth by implementing an analog chirp-transform algorithm using chirp filters [1],[2]. Superwideband compressive receivers utilizing high-temperature superconductive (HTS) chirp filters were demonstrated with 4-GHz instantaneous analysis bandwidth, well beyond the 1-GHz limit of conventional compressive receivers based on surface acoustic wave chirp filters [3]. Superwideband compressive receivers have a sensitivity advantage over other receiver technologies [1]. They also have a size, weight, and power advantage deriving from the wide analysis bandwidth per channel and the low-power high-speed digital back end enabled by advances in semiconductor technology [4]. HTS technology, which enables compact stripline with very low conductor propagation loss, was used to achieve 40-ns and potentially longer chirp-filter delays. The effort described here on 16-ns-long normal-metal (gold) chirp filters demonstrates filter performance sufficient for electronic warfare applications [1]–[3] using noncryogenic filter technology.

Figure 6-1(a) shows the layout and illustrates the operation of a proximity-tapped electromagnetic chirp filter. The chirp filters are based on a stripline configuration that uses two symmetrically placed ground planes on opposite sides of a pair of wafers. As a result, the packing density of the filter's tapped delay lines, and therefore the total chirp-filter length, are directly proportional to the thickness of the two wafers [3]. The normal-metal filters described here have been fabricated using 20-mil-thick 3-in-diam alumina substrates, which limited the total filter length to 16 ns. Figure 6-1(b) illustrates tap compensation for conductor propagation loss. A chirp-filter bandwidth  $B_c = 2.0$  GHz was chosen to match the chirp slope of an existing linear microwave chirp generator [5] so that actual compressed pulses could be generated in the laboratory, simulating the front end of a compressive receiver.

Figure 6-2(a) shows the transmission frequency response of a 2-GHz-bandwidth 16-ns-long Hamming-weighted gold-on-alumina downchirp filter. Tap compensation has been used to overcome the conductor propagation loss and recover the Hamming weighting. Parameters used in the theoretical plot were effective dielectric constant  $\epsilon_{\text{eff}} = 9.57$ , conductor propagation loss  $\alpha_c(f) = 0.80 \text{ Np/m-GHz}^{1/2} \times f^{1/2}$  where  $f$  is frequency in GHz, and total chirp-filter dispersive delay  $T = 15.6$  ns. The effective dielectric constant is reduced somewhat below the dielectric constant of the high-purity alumina ( $\epsilon = 9.9$ ) because of the presence of air gaps on either side of the 4- $\mu\text{m}$ -thick gold signal lines. The dielectric propagation loss  $\alpha_d(f) = 3.2 \times 10^{-3} \text{ Np/m-GHz} \times f$ , where  $f$  is frequency in GHz, for  $\tan \delta = 10^{-4}$  in the alumina substrate is negligible compared to the conductor propagation loss of the gold. The uncompensated theoretical curve in Figure 6-2(a) shows the effect of propagation loss on a downchirp filter designed with Hamming weighting

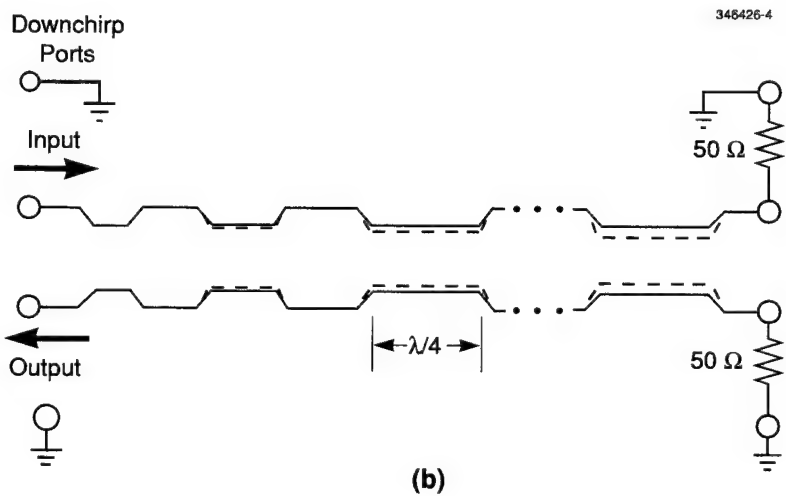
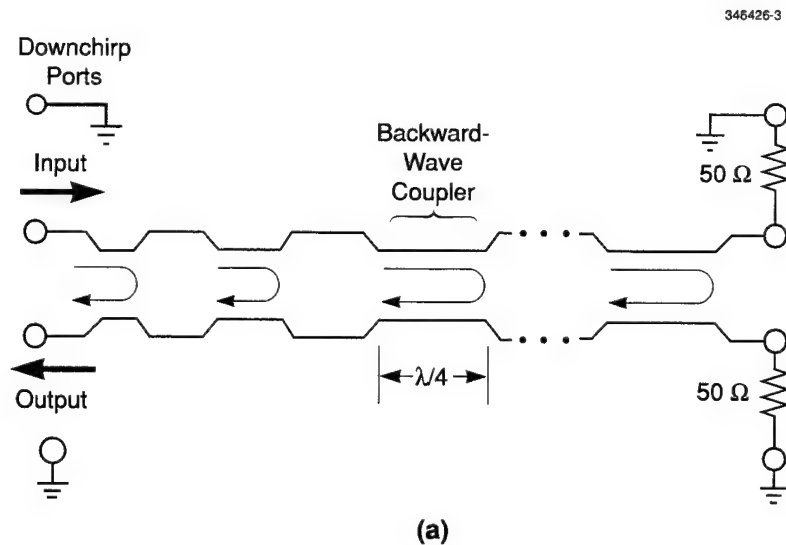


Figure 6-1. (a) Layout and operation of proximity-tapped electromagnetic chirp filter. The filter is shown here as flat weighted and configured as a downchirp filter with the upchirp ports terminated into 50-Ω loads. The electromagnetic delay lines are implemented in stripline, and a cascade of backward-wave couplers implements the taps. (b) Tap strength can be increased to compensate for normal-metal (gold) conductor propagation loss. The requirement of weak coupling for all taps to avoid distorting the input signal sets a limit on the amount of compensation.

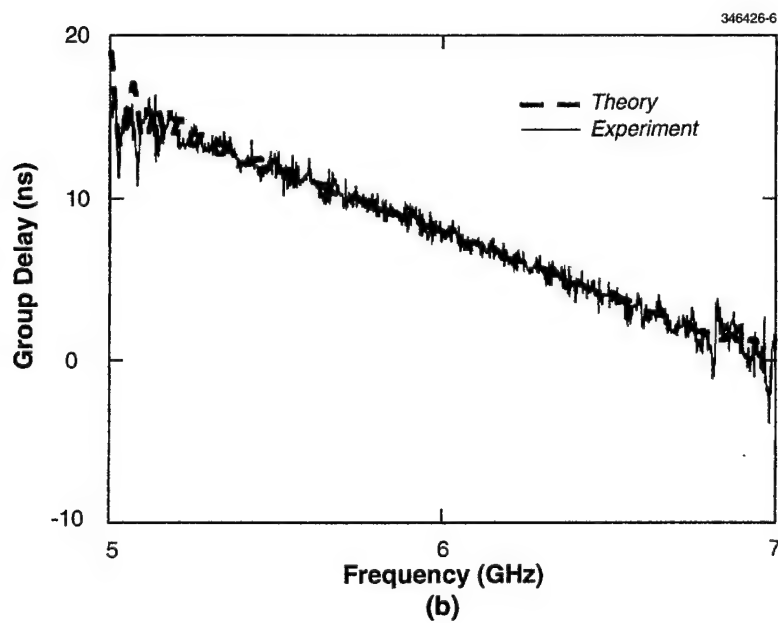
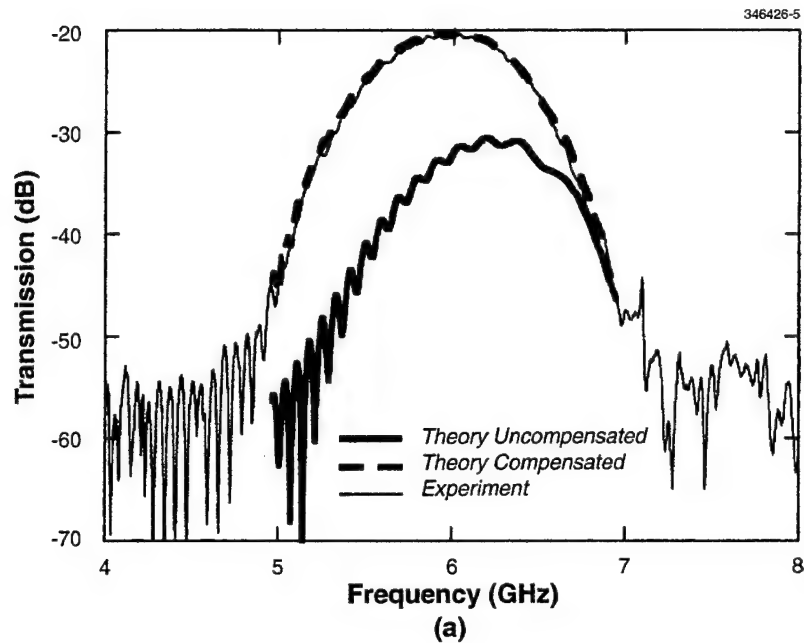


Figure 6-2. Frequency response of 2-GHz-bandwidth 16-ns-long Hamming-weighted gold-on-alumina chirp filter: (a) transmission ( $S_{21}$ ) vs frequency and (b) group delay vs frequency, both measured using the (compensated) downchirp ports of the filter. Measured data is shown along with the theoretical response. Note the linear downchirp group delay vs frequency characteristic. A curve also shows the theoretical transmission vs frequency response for an uncompensated filter.

and 20-dB insertion loss, assuming no propagation loss in the design. Figure 6-2(b) shows the measured and theoretical group delay vs frequency for the compensated normal-metal downchirp filter. Agreement between measurement and theory is again good.

A measure of the accuracy of the chirp filter is to operate the filter in a chirp-transform configuration with a linear chirp generator that is equally or more accurate than the chirp filter [5]–[7]. Paired echo theory quantifies how deviations from a linear chirp, particularly periodic deviations, in either the generated chirp signal or the matched chirp-filter compressor will result in “false” compressed-pulse mainlobes whose amplitude depends on the magnitude of the phase or amplitude deviations [8]. These false mainlobes are termed error sidelobes and may appear above the ideal sidelobe levels set by weighting in the filter. For example, the first ideal sidelobe for Hamming weighting is –43 dB below the mainlobe. Error sidelobes –40 dB below the mainlobe require less than ~1% periodic phase and amplitude errors in the chirp-generator/chirp-filter combination. Error sidelobes determine the two-tone dynamic range performance of a compressive receiver.

The analog chirp-transform front end of a compressive receiver provides the instantaneous Fourier power spectrum over the analysis band during each analysis window. For this demonstration, 2-GHz-bandwidth 15.6-ns normal-metal chirp filters have been used to overscan a 6-GHz analysis band during a 46.8-ns analysis window, thereby overscanning an input bandwidth wider than 2.0 GHz at the expense of reduced time coverage (25%). The input signal frequencies span the band from 8.0 to 14.0 GHz. The linear microwave chirp generator sweeps from 13.0 to 21.0 GHz to produce an 8.0-GHz 63-ns-long upchirp signal. Each signal at the input is mixed against this upchirp signal, and the resulting upchirp signal is compressed in the downchirp filter to become a 0.67-ns (at –3-dB points) compressed pulse at the output. The output time of the compressed pulse is related to the input-signal frequency, and the compressed-pulse amplitude represents the input-signal amplitude. Figure 6-3 shows the results of such a chirp-transform operation on an 11.6-GHz input signal. The frequency response of the filter was shown in Figure 6-2. This chirp-generator/chirp-filter combination produced far-out error sidelobes ~42 dB below the mainlobe peak. The pulsewidth of the compressed-pulse mainlobe is  $W_{cp} = k/B_c = 0.67$  ns, where  $k = 1.33$  for Hamming weighting and  $B_c = 2.0$  GHz for the filter. The 20-ns time window shown in Figure 6-3 corresponds to 30 compressed-pulse pulsewidths. The frequency resolution for this chirp transform is  $\Delta f = k/T = 85$  MHz, where  $k = 1.33$  and total chirp-filter dispersive delay  $T = 15.6$  ns. The full analysis window was 70 pulsewidths long (46.8 ns) in this overscan mode covering a 6-GHz input bandwidth.

This demonstration with normal-metal chirp filters of error sidelobes more than 40 dB below the mainlobe peak is a significant technical milestone. The normal-metal chirp filters demonstrated here have comparable performance to the best HTS chirp filters produced to date [9].

W. G. Lyons	D. J. Baker
G. L. Fitch	E. M. Macedo
P. G. Murphy	A. C. Anderson
R. R. Boisvert	

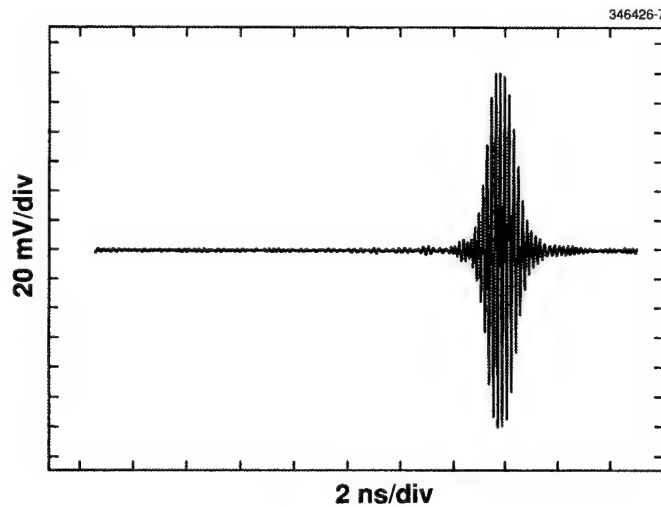


Figure 6-3. Measured compressed-pulse response of linear microwave upchirp generator and normal-metal downchirp filter combination. An input signal at 11.6 GHz resulted in this chirp-transform output. The far-out error sidelobes are more than  $\sim 42$  dB down from the mainlobe peak.

#### REFERENCES

1. K. D. Breuer, J. S. Levy, and H. C. Paczkowski, *Microwave J.* **32** (10), 81 (1989).
2. J. B.-Y. Tsui, *Microwave Receivers with Electronic Warfare Applications* (Krieger, Malibu, Fla., 1992).
3. W. G. Lyons, D. R. Arsenault, A. C. Anderson, T. C. L. G. Sollner, P. G. Murphy, M. M. Seaver, R. R. Boisvert, R. L. Slattey, and R. W. Ralston, *IEEE Trans. Microwave Theory Tech.* **44**, 1258 (1996).
4. R. Berger, W. G. Lyons, and A. Soares, *IEEE J. Solid-State Circuits* **33**, 1259 (1998).
5. Solid State Research Report, Lincoln Laboratory, MIT, 1998:2, p. 41.
6. P. J. Burke, *MTT-S International Microwave Symposium Digest* (IEEE, Piscataway, N.J., 1994), Vol. 2, p. 957.
7. J. Levy, P. J. Burke, L. D. Cohen, and R. Cecchini, *MTT-S International Microwave Symposium Digest* (IEEE, Piscataway, N.J., 1993), Vol. 2, p. 1113.
8. C. E. Cook and M. Bernfeld, *Radar Signals: An Introduction to Theory and Application* (Academic, New York, 1967).
9. W. G. Lyons, unpublished material.

## 7. ADVANCED SILICON TECHNOLOGY

### 7.1 THREE-DIMENSIONAL CIRCUIT INTEGRATION TECHNOLOGY FOR MULTIPROJECT FABRICATION

Conventional integrated circuits comprise a single layer of transistors interconnected with multiple layers of metal wiring. The density, speed, and power dissipation of these two-dimensional (2D) devices are increasingly limited by the wiring, providing strong motivation to take advantage of the third dimension. Three-dimensional integrated circuits (3D-ICs) composed of active circuit layers that are vertically stacked allow much shorter interconnect paths and hence are expected to lead to improved logic devices, memories, CPUs, and photosensors [1]. These circuits will require high-density vertical interconnections (3D vias) comparable in aspect ratio to present multilevel metal vias [2]. We report promising results from such 3D-ICs fabricated in a collaboration with Northeastern University and Kopin Corporation. Building on this work, a new program to establish a robust 3D circuit integration technology suitable for commercial transfer and multiproject run fabrication has been initiated in collaboration with industry. The initial goals of the new program are to consolidate 3D integration technology development efforts within Lincoln Laboratory, create a set of design rules tailored to 3D circuits, and fabricate a monochromatic, high-resolution  $1024 \times 1280$  visible imager with  $10\text{-}\mu\text{m}$  pixel pitch, on-chip analog-to-digital (A/D) conversion, and on-chip digital signal processing. This sensor will consist of three stacked and interconnected silicon circuits: a photodiode layer, an A/D converter layer, and a signal processing layer.

Three-dimensional ring oscillators and back-illuminated  $64 \times 64$  active pixel sensors have been fabricated using two vertically stacked wafers and found to function correctly. Each pixel of the imager comprises a photodiode on one wafer and an A/D converter on the other wafer. The oscillator consists of inverters alternating between wafers; that is, an inverter in one wafer is followed by the next inverter in the other wafer. Silicon-on-insulator (SOI) wafers are used to achieve stacking of multiple circuit layers and unrestricted placement of 3D vias.

The construction of these circuits consists of bonding and interconnecting an SOI wafer with imaging circuits to an SOI wafer with pixel-parallel A/D converter circuits. The imager circuits were fabricated in a  $10\text{-}\mu\text{m}$  epitaxial silicon layer on a  $0.3\text{-}\mu\text{m}$  bonded and etched back SOI layer with a  $1\text{-}\mu\text{m}$  buried oxide (BOX). The epi thickness was chosen for good optical performance in the visible and near-infrared spectrum. The A/D circuits were fabricated in a  $1\text{-}\mu\text{m}$  SOI layer with a  $1\text{-}\mu\text{m}$  BOX. Both wafers were processed with the same two-level metal  $0.8\text{-}\mu\text{m}$  CMOS process designed to operate at 5 V. Prior to CMOS fabrication, silicon trenches were etched through the SOI layer of the A/D wafer and filled with deposited oxide to form channels through which 3D vias would be etched to interconnect the two active layers.

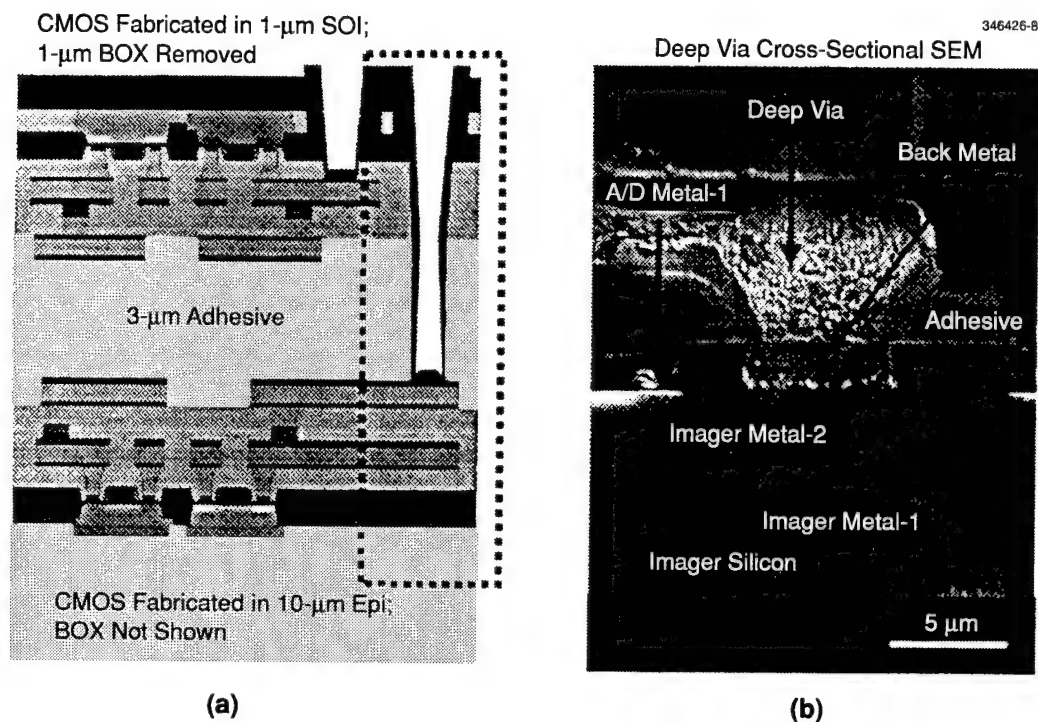


Figure 7-1. (a) Diagram of bonded analog-to-digital (A/D) (top) and imager integrated circuit layers, and (b) scanning electron micrograph cross section of a deep via.

The 3D stacking and via structure are illustrated in Figure 7-1. After wafer fabrication and test, the A/D wafer was inverted, aligned to the imager wafer using an infrared aligner, and bonded with a 3- $\mu\text{m}$ -thick adhesive. Then the bulk silicon was etched from the A/D wafer to expose the BOX. The BOX was used as a stop for the silicon etch to produce a thin, uniform active layer and is an essential step in the 3D assembly technology. A set of shallow 3D vias was etched through the BOX, trench, and deposited oxides of the A/D wafer to expose metal pads on the first metal layer of the A/D wafer. A deep set of 3D vias was defined and etched entirely through the A/D wafer plus the adhesive, to expose metal pads on the second metal layer of the imager wafer. The 3D vias were 6  $\mu\text{m}$  square and were 2.7 and 7.5  $\mu\text{m}$  deep for the shallow and deep vias, respectively. An aluminum alloy was deposited by bias sputtering and defined to connect the metal pads of the two wafers. The assembly was inverted and bonded to an oxidized silicon wafer for mechanical support, and the handle silicon was etched from the imager wafer to expose the epi layer for back-side imaging. Bond pads were defined and etched through the 10- $\mu\text{m}$  silicon and the BOX to expose pads on the first metal layer of the imager. The assembly was diced into chips and packaged; then the characteristics of active pixel sensors, ring oscillators, and test structures were determined.

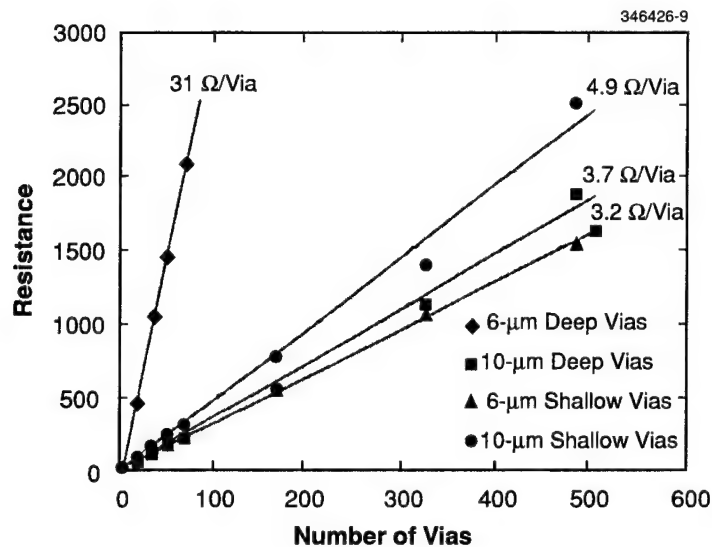


Figure 7-2. Resistances of shallow and deep via chains.

The resistances of shallow and deep via chains are shown in Figure 7-2 along with the size of the 3D vias. The 10- $\mu\text{m}$ -square deep and shallow via resistances are comparable, indicating that etching through the adhesive did not degrade the contact either by undercutting the adhesive bond or by contaminating the metal pad from adhesive residue. The increased resistance of the 6- $\mu\text{m}$  deep vias is caused by a reduction of the via contact area due to shadowing during sputter cleaning.

Three-dimensional ring oscillators were constructed by coupling an inverter from the imager wafer to an inverter in the A/D wafer with 3-, 6-, or 10- $\mu\text{m}$  3D vias. 2D ring oscillators were also fabricated in the imager and A/D circuit wafers. The layout of a 3D ring oscillator is shown in Figure 7-3, and the delays per stage are shown in Figure 7-4. The delays of 2D and 3D devices with 6- and 10- $\mu\text{m}$  deep vias are equal indicating the 3D via design and fabrication process did not degrade the performance of the ring oscillators. Ring oscillators with 3- $\mu\text{m}$  deep vias were included to determine the limits of the epoxy-bond process since the current design rules limit the deep via size to a minimum of 6  $\mu\text{m}$ . The ring oscillator delays are characteristic of capacitively coupled vias, and measurements of 3- $\mu\text{m}$  deep via chains, not shown, indicated that those vias are open.

The sensor chip contains 4096 pixels; in each pixel an optical signal is generated by an  $n^+/p$  diode in the imager wafer and is coupled to a CMOS circuit in the A/D wafer through a 6- $\mu\text{m}$  deep via. The A/D circuit periodically resets the potential of the photodiode and produces an output proportional to the

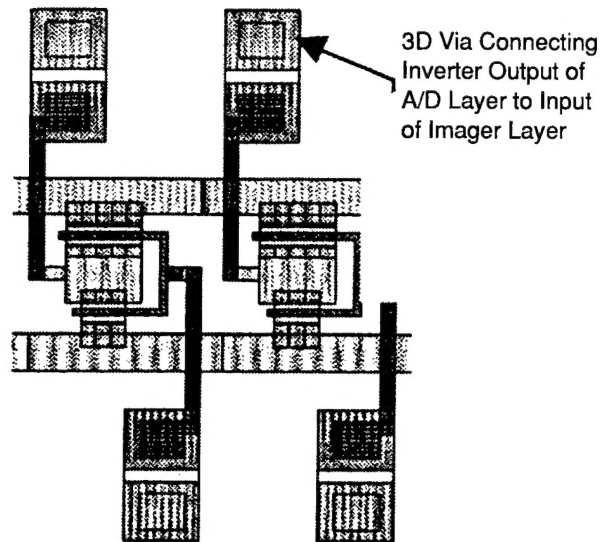


Figure 7-3. Layout of A/D layer of three-dimensional (3D) ring oscillator, showing the pads used to connect the two active layers with 3D vias.

photodiode current. Five sensor chips were packaged, installed in a camera, and tested. The images shown in Figure 7-5 were obtained from the first sensor tested. While there are some white pixels due to high local dark current and some dark pixels due to excessive leakage in the reset transistor, we believe these results to be the first demonstration of the successful fabrication of a complex 3D circuit.

The performance of these 3D ring oscillators and active pixel sensors have shown the feasibility of stacking SOI circuits to build 3D-ICs. Advanced systems such as the planned  $1024 \times 1280$  sensor will require the stacking and interconnection of higher-performance CMOS circuits with higher-density 3D vias. The sensor's A/D and signal processing circuits will be fabricated using Lincoln's 180-nm fully depleted SOI technology to achieve both low power and high performance. The density of 3D vias will be increased by replacing the adhesive process with low-temperature oxide bonding, utilizing tungsten plugs to fill smaller vias, and developing improved wafer-to-wafer alignment and bonding equipment.

J. A. Burns

L. G. McIlrath\*

K. Warner

C. L. Keast

P. W. Wyatt

---

\*Author not at Lincoln Laboratory.

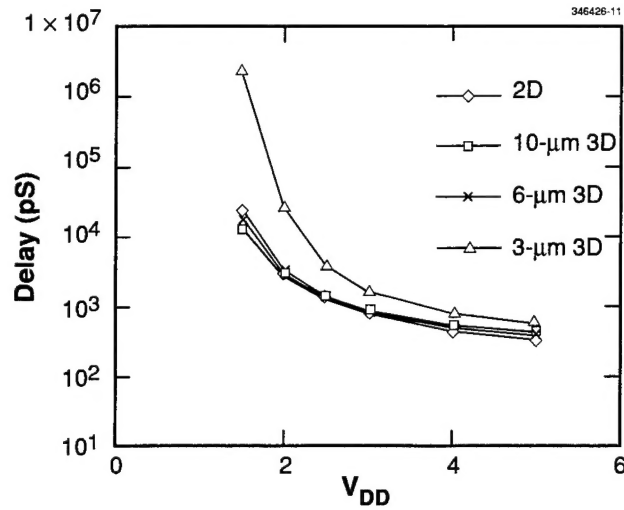


Figure 7-4. Delay per stage of 2D and 3D ring oscillators. The dimensions in the figure are the deep 3D via sizes.

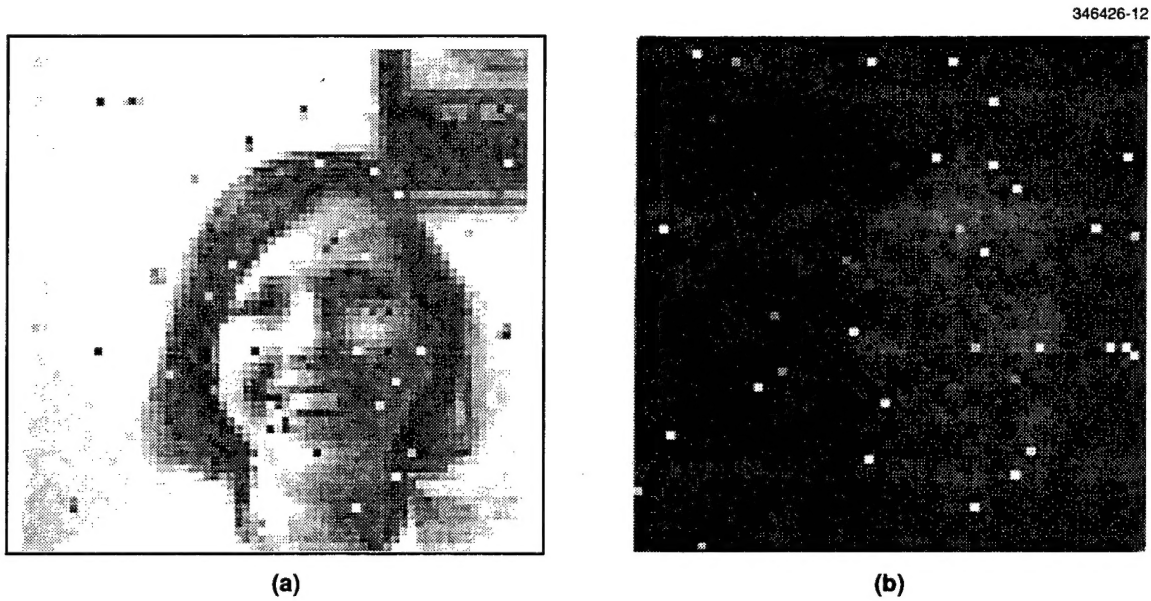


Figure 7-5. Images obtained from  $64 \times 64$  active pixel sensor with (a) normal and (b) near-infrared illumination. The photodiode signals generated in the imager layer are connected to asynchronous current-controlled relaxation oscillators in the A/D layer by  $6\text{-}\mu\text{m}$  deep 3D vias.

## REFERENCES

1. Y. Akasaka, *Proc. IEEE* **74**, 1703 (1986).
2. M. Reber and R. Tielert, *IEEE Symposium on Circuits and Systems* (IEEE, Piscataway, N.J., 1996), Vol. 4, p. 121.

